CMS PAPER CFT-09-002

FERMILAB-PUB-10-147-CMS

CMS Paper

2009/11/26

Commissioning and Performance of the CMS Silicon Strip Tracker with Cosmic Ray Muons

The CMS Collaboration*

Abstract

During autumn 2008, the Silicon Strip Tracker was operated with the full CMS experiment in a comprehensive test, in the presence of the 3.8 T magnetic field produced by the CMS superconducting solenoid. Cosmic ray muons were detected in the muon chambers and used to trigger the readout of all CMS sub-detectors. About 15 million events with a muon in the tracker were collected. The efficiency of hit and track reconstruction were measured to be higher than 99% and consistent with expectations from Monte Carlo simulation. This article details the commissioning and performance of the Silicon Strip Tracker with cosmic ray muons.

*See Appendix A for the list of collaboration members

1 Introduction

The primary goal of the Compact Muon Solenoid (CMS) experiment [1] is to explore particle physics at the TeV energy scale exploiting the proton-proton collisions delivered by the Large Hadron Collider (LHC) [2]. The central tracking detector [1] built for the CMS experiment is a unique instrument, in both size and complexity. It comprises two systems based on silicon sensor technology: one employing silicon pixels and another using silicon microstrips. The Pixel Detector surrounds the beampipe and contains 66 million detector channels [3]. The Pixel system is, in turn, surrounded by the Silicon Strip Tracker (SST), which is the subject of this paper.

The SST consists of four main subsystems, shown in Fig. 1: the four-layer Tracker Inner Barrel (TIB), the six-layer Tracker Outer Barrel (TOB) and, on each side of the barrel region, the three-disk Tracker Inner Disks (TID), and the nine-disk Tracker End Caps (TEC). Each TID disk is made of three rings of modules, while TEC disks have seven rings. Overall, the tracker cylinder is 5.5 m long and 2.4 m in diameter, with a total active area of 198 m^2, consisting of 15 148 detector modules and comprising 9.3 million detector channels. Each detector module consists of a carbon or graphite fibre frame, which supports the silicon sensor and the associated front-end readout electronics. Four barrel layers and three rings in the end cap disks are equipped with double-sided modules, each of which is constructed from two single-sided modules mounted back-to-back with a stereo angle of 100 mrad between the strips. The silicon sensors are made up of single-sided p^+ strips on n-bulk sensors with two different thicknesses: 320 μm and 500 μm in the inner four and outer six layers of the barrel, respectively; 320 μm in the inner disks; and 320 μm and 500 μm in the inner four and outer three rings of the end cap disks, respectively. There are a total of fifteen different types of sensors in the SST, which vary in terms of strip length and pitch [4] to ensure that the single strip occupancy is low even at full LHC luminosity.

The first experience of the SST operation and detector performance study was gained in summer 2006, when a small fraction of the SST was inserted into the CMS detector. Cosmic ray

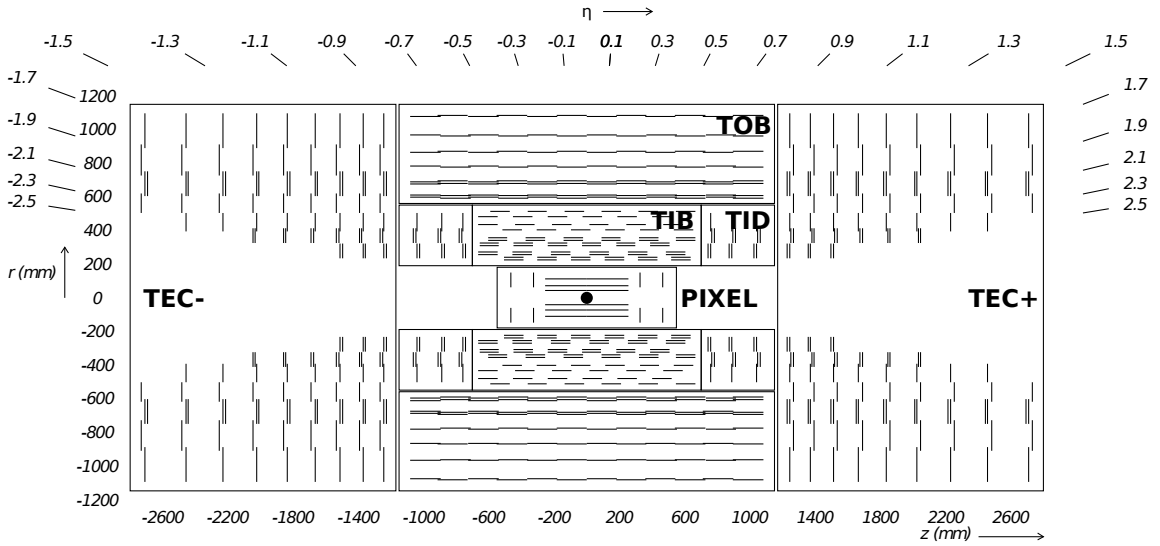

Figure 1: Schematic cross section of the CMS tracker. Each line represents a detector module. Double lines indicate double-sided modules which deliver stereo hits.

muon data were recorded in the presence of a solenoidal field up to the maximum design value of 4 T. The results from this period of data-taking are described elsewhere [5]. Construction of the full SST was completed in 2007 and 15% of the full SST was commissioned and operated for several months prior to installation in the underground CMS experimental hall. The results of this period of stand-alone operation, known as the Slice Test, are also described elsewhere [6, 7].

The installation of the SST within CMS was completed during 2008 and the system underwent its first round of *in situ* commissioning together with the other CMS sub-detectors during summer 2008. The first operation of the SST in a 3.8 T magnetic field took place during October-November 2008, when the CMS Collaboration conducted a month-long data-taking exercise known as the Cosmic Run At Four Tesla (CRAFT) [8]. This exercise provided valuable operational experience, as well as allowing, for the first time, a full study of the SST performance after installation. First results from the study are presented here.

This paper is laid out as follows. The procedures used to commission the SST and the results from the round of *in situ* commissioning are presented and discussed in Section 2. The final data samples from CRAFT and the corresponding Monte Carlo simulations are described in Section 3. The performance results obtained from the CRAFT data samples for hit and track reconstruction are presented in Sections 4 and 5, respectively.

2 Commissioning the SST Control and Readout Systems

In order to bring the SST detector into an operational state suitable for data-taking, several commissioning procedures are required to checkout, configure, calibrate, and synchronise the various hardware components of the control and readout systems. The majority of the commissioning procedures are performed with the SST operating independently of the rest of the CMS experiment. Only the procedures that concern synchronisation to an external trigger, described in Section 2.7, require reconstructed particle trajectories from cosmic ray muons or LHC pp collision data. The commissioning of the SST aims to maximise the signal identification efficiency for in-time particles and minimise pileup due to out-of-time particles. The ultimate objective is to maximise the tracking efficiency while minimising the number of tracks caused by out-of-time signals from adjacent bunch crossings.

Section 2.1 provides an overview of the SST control and readout systems. Section 2.2 summarises the checkout procedures used to determine the functional components of these systems. Sections 2.3-2.7 review the various commissioning procedures and their performances.

2.1 The control and readout systems

The major components of the SST readout system [9] are: 15 148 front-end detector modules that host 76 000 APV25 [10] readout chips, an analogue optical link system comprising 38 000 individual fibres [11], and 440 off-detector analogue receiver boards, known as Front-End Drivers (FED) [12]. The SST control system [13] is driven by 46 off-detector digital transceiver boards, known as Front-End Controllers (FEC) [14]. The FECs distribute the LHC clock, triggers and control signals to the front-end detector modules via Communication and Control Units (CCU) [15], which are hosted on 368 *control rings*.

The APV25 readout chip samples, amplifies, buffers, and processes signals from 128 detector channels at a frequency of 40 MHz. Fast pulse shaping is therefore required to provide bunch crossing identification and minimise pileup. This is difficult to achieve with low noise and power levels, so the APV25 chip uses pre-amplifier and shaper stages to produce a CR-RC pulse shape with a relatively slow rise-time of 50 ns in an operating mode known as *peak*. An

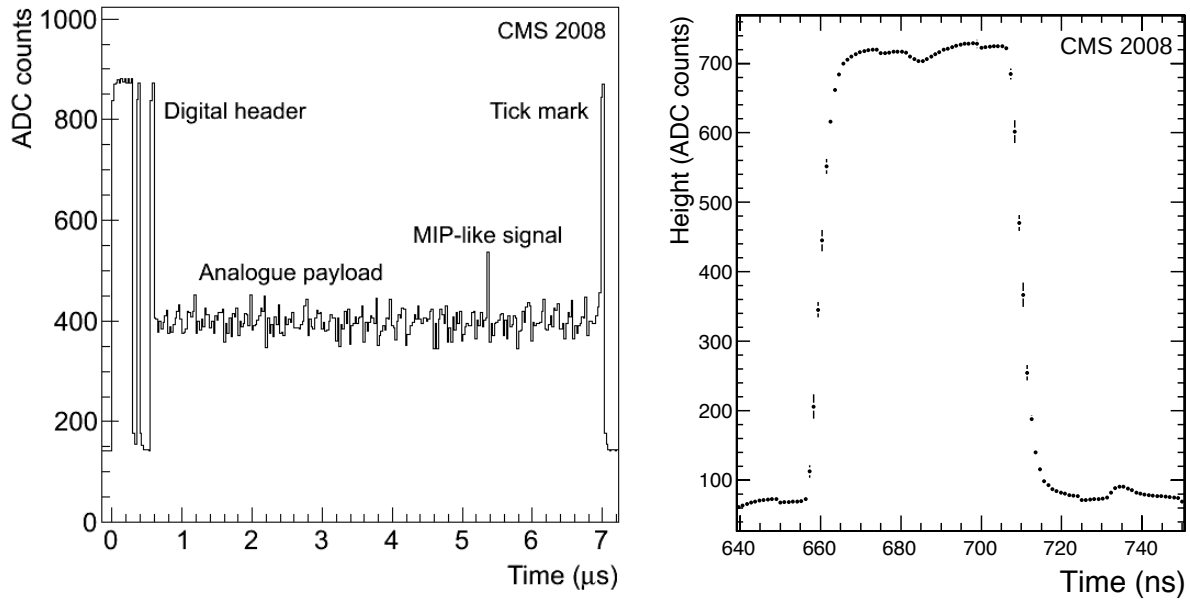

Figure 2: (left) Two APV25 data frames multiplexed, containing a time stamp and the sensor pulse height information. (right) A feature of the APV25 data stream, known as a tick mark, that is heavily used by the checkout and commissioning procedures. The left and right figures have sampling intervals of 25 ns and 1.04 ns, respectively.

alternative mode, *deconvolution*, performs additional signal processing to constrain the signal to a single bunch crossing [16] at the expense of a reduced signal-to-noise ratio. Deconvolution is expected to be the standard mode of operation. However, the results presented in this paper are based on data accumulated with peak mode operation, unless stated otherwise.

Figure 2 (left) shows an example of the raw data captured at 40 MHz by a single FED readout channel on receipt of a trigger. The data contain frames from two APV25 chips that are multiplexed (interleaved) together. A single frame comprises 12 bits of binary information that encodes time and error information, known as the digital header, followed by analogue pulse height data from 128 sensor strips. A trailing *tick mark* identifies the end of the frame. The structure observed in the pulse height data across the 128 channels is due to static offsets, known as *pedestals*, which are unique to each detector channel. Small, time-varying *common mode* shifts in the levels of all 128 channels are observed when operating. Figure 2 (left) also shows an example of a signal left by a minimum ionising particle. Signals are superimposed on the pedestal and common mode levels, which must be subtracted before the signal can be identified.

In the absence of a trigger, no data frames are output by the APV25 chip, but tick marks are produced every 70 clock cycles. Figure 2 (right) shows the pulse shape of multiplexed tick marks from two APV25 chips that are reconstructed with an effective sampling frequency of 960 MHz. This tick mark feature is used heavily in the checkout and commissioning procedures detailed below.

The FEDs can format the pulse height data from the APV25 chips in different ways. The first is Scope Mode (SM), which is simply a capture of the raw data, as shown in Fig. 2 (left). The second is Virgin Raw (VR), which removes all of the binary information (digital header and tick marks) and simply provides the digitised pulse height data from the sensors. Both modes provide digital samples with a 10-bit range and are used when commissioning the SST system and for debugging. The third and normal mode of operation is Zero Suppressed (ZS). This uses

Field Programmable Gate Array (FPGA) chips to implement algorithms that perform pedestal subtraction, common mode subtraction, and identification of channels potentially containing signals above threshold. A threshold of five times the detector channel noise is used for single channels, but a threshold of only twice the channel noise is used for signals in contiguous channels. The zero-suppressed data are output with an 8-bit range.

2.2 Checkout of the detector components and cabling

The checkout procedures are used to identify: responsive and functional devices in the control and readout systems; the cabling of the readout electronics chain, from the front-end detector modules to the off-detector FED boards; the cabling of the Low Voltage (LV) and High Voltage (HV) buses of the power supply system [17]; and the mapping of the detector modules to their geometrical position within the SST superstructure. Automation is possible as each detector module hosts a Detector Control Unit (DCU) chip [18], which broadcasts a unique indentifier via the control system. This identifier is used to tag individual modules.

The cabling of the LV power supply system is established by sequentially powering groups of detector modules and identifying responsive devices via the control system. Similarly, the HV cabling is determined by applying HV to an individual channel and identifying detector modules responding with a decreased noise, due to reduced strip capacitance.

Each front-end detector module hosts a Linear Laser Driver (LLD) chip [19], which drives the optical links that transmit the analogue signals to the off-detector FED boards. The cabling of the readout electronics chain is established by configuring individual LLD chips to produce unique patterns in the data stream of the connected FED channels.

The final number of modules used in the CRAFT data-taking period corresponds to 98.0% of the total system. The most significant losses were from one control ring in each of the TIB and TOB sub-systems. In the TIB, this was due to a single faulty CCU. The remaining CCUs on this ring have since been recovered using a built-in redundancy feature of the control ring design. The fraction of operational modules was increased to 98.6% after data-taking, once problems identified during checkout were investigated more fully.

2.3 Relative synchronisation of the front-end

Relative synchronisation involves adjusting the phase of the LHC clock delivered to the front-end so that the sampling times of all APV25 chips in the system are synchronous. Additionally, the signal sampling time of the FED Analogue/Digital Converters (ADC) is appropriately adjusted. This procedure accounts for differences in signal propagation time in the control system due to differing cable lengths. This synchronisation procedure is important because signal amplitude is attenuated by as much as 4% per nanosecond mis-synchronisation due to the narrow pulse shape in deconvolution mode.

Using the FED boards in Scope Mode, the tick mark pulse shape is reconstructed with a 1.04 ns step width by varying the clock phase using a Phase Locked Loop (PLL) chip [20] hosted by each detector module, as shown in Fig. 2 (right). The ideal sampling point is on the signal plateau, 15 ns after the rising edge of the tick mark. The required delays are thus inferred from the arrival times of the tick mark edges at the FED ADCs. The pre-synchronisation timing spread of up to 160 ns is reduced to an RMS of 0.72 ns, with the largest deviation of 4 ns corresponding to a maximum signal attenuation of $\sim$16% in deconvolution mode.

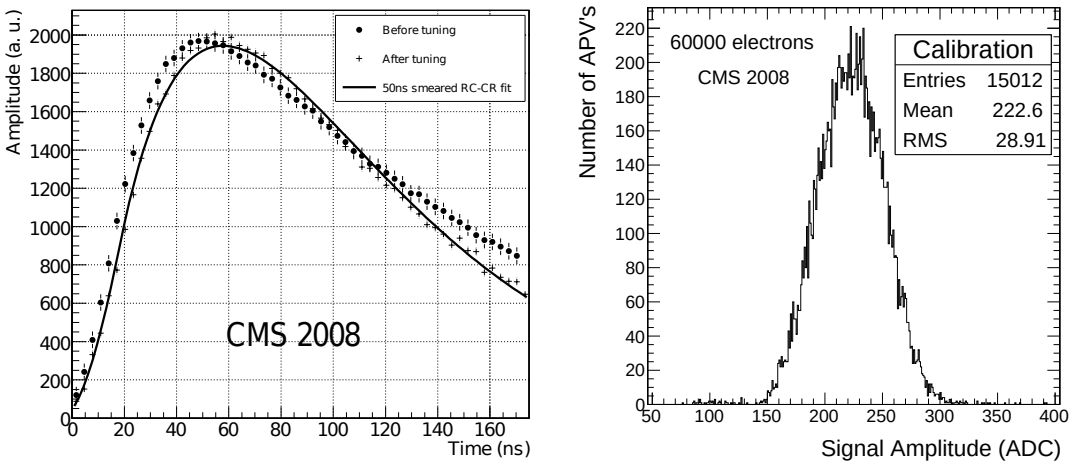

Figure 3: (Left) An example of the CR-RC pulse shape of a single APV25 chip, before and after the pulse shape tuning procedure. (Right) Pulse height measurements using the on-chip calibration circuitry of APV25 chips in the TEC+.

2.4 Calibration of the readout system gain

One of the largest contributions to gain variation in the readout system is the distribution of laser output efficiencies caused by the variation of laser-to-fibre alignment from sample to sample during production of the transmitters. In addition some loss may have been introduced at the three optical patch panels in the fibre system. Changes in the LV power supply or environmental temperature can also significantly affect the gain at the level of a FED readout channel.

The calibration procedure aims to optimise the use of the available dynamic range of the FED ADCs and also equalise the gain of the entire readout system. This is achieved by tuning the bias and gain register settings of the LLD chip for individual fibres. Four gain settings are possible. The amplitude of the tick mark, which is assumed to be roughly constant in time and across all APV25 chips within the system, is used to measure the gain of each readout channel. The setting that results in a tick mark amplitude closest to 640 ADC counts is chosen, as this amplitude corresponds to the expected design gain of 0.8. After tuning the system, a spread of $\pm 20\%$ is observed, which is expected because of the coarse granularity of the LLD gain settings.

The response of all detector channels can be further equalised during offline reconstruction by correcting the signal magnitude by the normalisation factor $f = 640$ ADC counts $/a_{\text{tickmark}}$, where a_{tickmark} is the tick mark amplitude in ADC counts. The tick mark amplitude is a good indicator of the maximum output of the APV25 chip, which corresponds to a charge deposit of 175 000 e^-. This method provides a calibration factor of 274 ± 14 e^-/ADC count. The estimated systematic uncertainty is 5%, attributable to the sensitivity of the tick mark amplitude to variations in the LV power supply and environmental temperature [6].

2.5 Tuning of the APV25 front-end amplifier pulse shape

The shape of the CR-RC pulse from the APV25 pre-amplifier and shaper stages is dependent on the input capacitance, which depends on the sensor geometry and evolves with total radiation dose. By default, all APV25 chips are configured with pre-defined settings appropriate to the sensor geometry, based on laboratory measurements [21]. However, non-uniformities in the fabrication process result in a small natural spread in the pulse shape parameters for a given input capacitance. This issue is important for performance in deconvolution mode, which is sensitive to the CR-RC pulse shape. In order to maximise the signal-to-noise ratio and con-

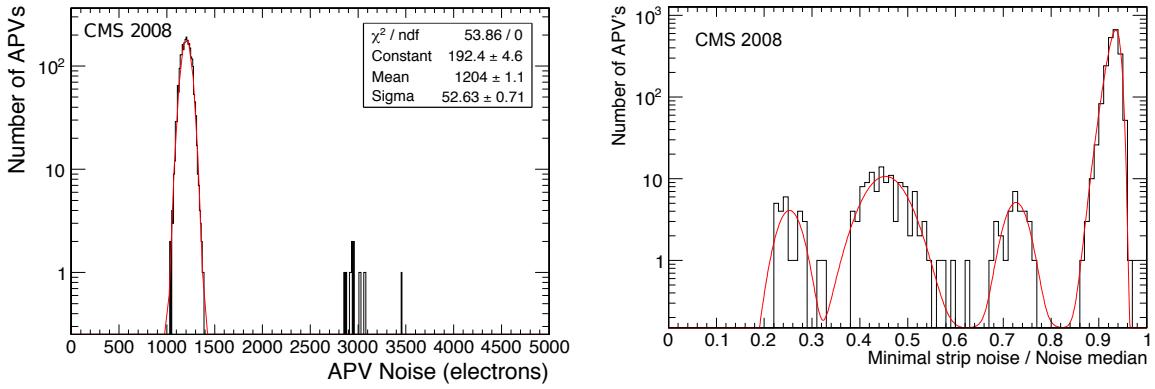

Figure 4: (Left) Mean calibrated noise for individual APV25 chips on modules in the TOB single side layer 3. (Right) The ratio of minimum noise to median noise per APV25 chip. The distinct populations reflect the different noise sources within a module.

fine the signal to a single bunch crossing interval when operating in deconvolution mode, the rise time of the CR-RC pulse shape must be tuned to 50 ns and the signal amplitude at 125 ns after the signal maximum should be 36% of the maximum. This tuning also reduces the timing uncertainties associated with the synchronisation procedures. Figure 3 (left) demonstrates how the CR-RC pulse shape of an APV25, operating in peak mode, can be improved by the procedure.

Figure 3 (right) shows the pulse height amplitude (in ADC counts) observed for a charge injection of 60 000 e^- using the on-chip calibration circuitry of the APV25 chip. The charge injection provided by the calibration circuit is known with a precision of 5% and can be used to calibrate the detector signal amplitude. A mean signal of 223 ADC counts with a RMS of 29 ADC counts was observed, giving a calibration factor of $269 \pm 13\,e^-$/ADC counts. This measurement is compatible with the calibration based on tick mark amplitudes, described in Section 2.4.

2.6 Calibration of the detector channel pedestals and noise

The mean level of the pedestals for the 128 channels of a given APV25 chip, known as the *baseline* level, can be adjusted to optimise the signal linearity and the use of the available dynamic range of the APV25. The baseline level for each APV25 chip is adjusted to sit at approximately one third of the dynamic range.

Following this baseline adjustment, the pedestal and noise constants for each individual detector channel must be measured, as these values are used by the zero-suppression algorithms implemented in the FPGA logic of the FEDs. Pedestals and noise are both measured using a random, low frequency trigger (∼10 Hz) in the absence of signal. Pedestals are first calculated as the mean of the raw data in each detector channel from a large event sample. They are subsequently subtracted from the raw data values for each event. Common mode offsets are evaluated for each APV25 chip per event by calculating the median of these pedestal-subtracted data. The median value is then subtracted from each channel. The noise for each detector channel is then defined to be the standard deviation of the residual data levels, which can be calibrated using the measurements described in Sections 2.4 and 2.5. Figure 4 (left) shows a distribution of the mean noise measured per APV25 chip, for TOB single side layer 3. The outliers correspond to APV25 chips from modules with unbiased sensors, due to problems in the HV power supply.

Modules with different sensor geometries are studied separately to account for the different

Table 1: Summary of the mean normalised noise for each type of sensor geometry.

Partition	Strip length (cm)	Total noise (e^-)	Pitch adapter (e^-)	Bare APV (e^-)
TEC Ring 1	8.52	757	421	245
TEC Ring 2	8.82	791	434	265
TEC Ring 3	11.07	832	450	250
TEC Ring 4	11.52	843	437	257
TEC Ring 5	14.44	1024	461	265
TEC Ring 6	18.10	1097	513	270
TEC Ring 7	20.18	1146	510	258
TOB Layers 1-4	18.32	1184	583	254
TOB Layers 5-6	18.32	1205	538	261
TIB Layers 1-2	11.69	925	454	265
TIB Layers 3-4	11.69	851	445	256

strip lengths and pitch adapter layouts that affect the input capacitance. The mean normalised noise measured for the different sensor geometries are summarised in Table 1. Fitting the mean noise versus silicon strip length, the following parameterisation is obtained:

$$noise(\mathrm{e}^-) = (427 \pm 39) + (38.7 \pm 3.0) \times length(cm)$$

This is compatible with the measurement performed during the SST integration period, prior to installation [1].

The individual sources of noise on the detector module can be identified and measured by plotting the ratio of the minimum to the median noise value for each APV25, as shown in Fig. 4 (right) and summarised in Table 1. The ratio takes advantage of the fact that broken wire bonds on the detector modules effectively reduce the input capacitance to individual channels of the APV25 chips. Broken wire bonds can occur between (in ascending order of capacitance): the APV25 and pitch adapter; the pitch adapter and silicon sensor; and sensors in two-sensor modules. Fitting to the first three populations, corresponding to the previous broken wire configurations, provides an estimate of different noise contributions. The fourth population corresponds to modules with no broken wires.

2.7 Absolute synchronisation to an external trigger

The last two commissioning procedures concern the synchronisation of all modules in the SST with the Level-1 trigger of CMS. This was done using a dedicated trigger provided by the Muon Drift Tube sub-detector [22], based on a coincidence between centrally-located top and bottom chambers. The procedure requires track reconstruction and the analysis was performed offline [21]. Absolute synchronisation accounts for both the delays introduced by the hardware configuration and the effects due to the time-of-flight of particles.

The first of the two procedures is a coarse scan in time, in steps of 25 ns, by adjusting the latency between the trigger arrival and the sampling time of the APV25 chip. The mean signal of the channel with the largest signal amplitude (*leading strip*) in clusters associated to reconstructed tracks was extracted as a function of the latency. The signal magnitude was corrected for the track path length through the active sensor volume, inferred from the track angle. The latency measurement was performed for the tracker as a whole, but fine adjustments for each partition were made relative to the TOB results: TIB and TEC- were shifted by 12.5 ns and TEC+ by -12.5 ns, as shown by the fits in Fig. 5 (left). Time-of-flight is not taken into account in this procedure, since the variations expected across the detector ($\leq$10 ns with cosmic ray muons, 5 ns in collisions) are lower than the target precision of 25 ns.

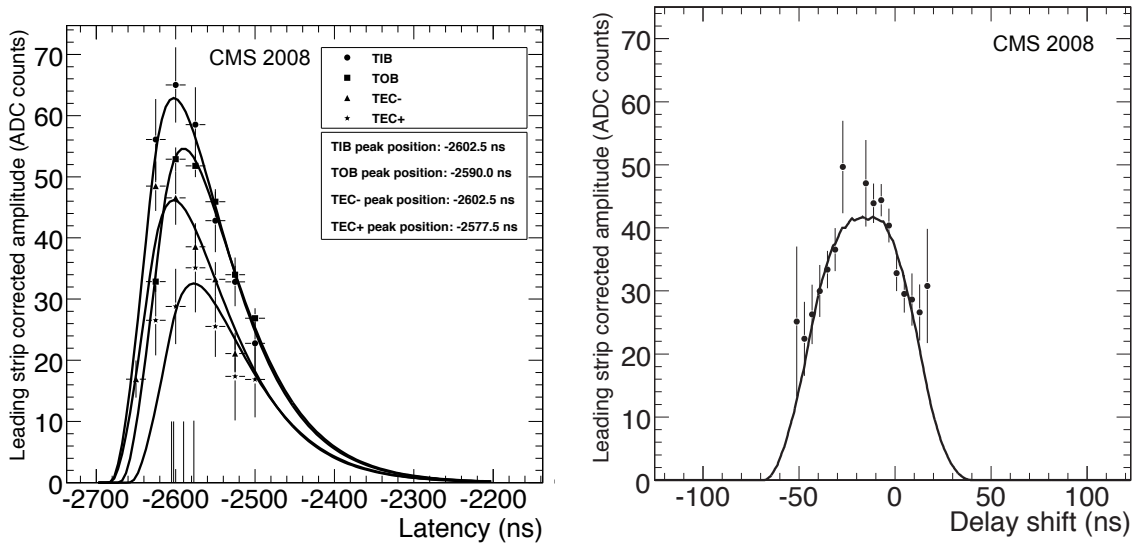

Figure 5: (Left) Mean signal of leading strip in clusters associated to tracks as a function of the latency (25 ns steps), for each of the four partitions. (Right) Fine delay scan for the TOB layer 3, in deconvolution. The mean position (-14.2 ns) is including the mean time-of-flight of particles from the muon system to the silicon sensors (12 ns).

The last procedure comprises a fine tuning of the synchronisation. It involves skewing the clock delay in steps of 1 ns around the expected optimal value for all modules of a given test layer, with the configuration of all other modules in the SST unchanged with respect to the value obtained from the coarse latency scan. Clusters on the test layer compatible with a reconstructed track are used to reconstruct the pulse shape. Figure 5 (right) shows the resulting pulse shape from clusters found in modules of TOB layer 3, acquired in deconvolution mode. With collision data, the time-of-flight can be adjusted for each individual track, but this is not the case for cosmic ray muons, for which the jitter from the trigger cannot be subtracted. The 14 ns shift observed is consistent with the expected time-of-flight (12 ns) of cosmic ray muons from the Muon Drift Tube chambers to the TOB layer 3.

From analysis of the latency and fine delay scans, correction factors are computed to compensate the residual mis-synchronisation of each partition. These corrections range from 1.0 to 1.06 with uncertainties of 0.03 and are used to correct the cluster charge in calibration and dE/dx studies, reported below.

3 Data Samples and Monte Carlo Simulations

In the following sections, the performance of the tracker will be analysed using the data collected during CRAFT. The event reconstruction and selection, data quality monitoring and data analysis were all performed within the CMS software framework, known as CMSSW [23]. The data quality was monitored during both the online and offline reconstruction [24]. The data were categorised and the results of this categorisation procedure propagated to the CMS Dataset Bookkeeping System [25]. Unless otherwise stated, only runs for which the quality was certified as good, i.e., no problems were known to affect the Trigger and Tracker performance, were used for the analyses presented in this paper.

The data-taking period can be split into three distinct intervals in time, based on magnetic field conditions and tracker performance. Each period has approximately uniform conditions. In

the first period, period A, part of the SST was not correctly synchronised with the rest of the CMS detector. This problem was fixed for data taken in subsequent periods. The magnet was at its nominal field value of 3.8 T during periods A and B, while period C corresponds to data taken with the magnet switched off. Unless stated otherwise, the following results are based only on events from period B.

For the studies presented in this paper, the events selected by the Global Muon Trigger [26] were used. This data sample was additionally filtered to include only events that contain at least one reconstructed track in the tracker or that have a track reconstructed in the muon chambers whose trajectory points back into the SST barrel volume.

Several analyses use a simulated sample of 21 million cosmic ray muons to derive correction factors and compare results. The sample was generated using the CMSCGEN package [27, 28]. The detector was simulated using the standard program of CMSSW. Modules known to be excluded from the read-out were masked in the simulation. Besides this, the simulation was not optimised to the conditions of CRAFT. Nevertheless, the agreement with the data was sufficient for the purpose of the studies presented.

4 Performance of the Local Reconstruction

In this section, the reconstruction at the level of the single detector module, is presented. The cosmic ray muon rate is small and events with more than one track are rare. So with zero-suppression only a tiny fraction of the SST channels are read out in any one event. These channels which pass zero-suppression and therefore have non-zero ADC counts are known as *digi*. Despite the zero suppression, digis may still only consist of noise.

Clusters are formed from digs by means of a three threshold algorithm [23]. Clusters are seeded by digis which have a charge that is at least three times greater than the corresponding channel noise. For each seed, neighbouring strips are added if the strip charge is more than twice the strip noise. A cluster is kept if its total charge is more than five times the cluster noise, defined as $\sigma_{\text{cluster}} = \sqrt{\sum_i \sigma_i^2}$, where σ_i is the noise from strip i, and the sum runs over all strips in the cluster.

In the following, the properties of both digis and clusters are studied and the performance of each SST subsystem is assessed.

4.1 Occupancy

The average number of digis per event and the occupancy are shown for each SST subsystem in Table 2. The strip occupancy is computed after removing the masked modules (2.0 %). The average occupancy in the SST is 4×10^{-4}, as expected from simulation and from the properties of the zero suppression algorithm. The digi occupancy is dominated by noise, but the cluster algorithm reconstructs less than ten hits per event when there is no track within the SST acceptance.

4.2 Signal-to-noise ratio

The signal-to-noise ratio is a benchmark for the performance of the SST. It is particularly useful for studying the stability over time. In the signal-to-noise ratio, the cluster noise is divided by $\sqrt{N_{\text{strips}}}$, so that the resulting noise value is approximately equal to the strip noise, independently of the size of the cluster. The path-length corrected signal-to-noise ratio distributions are presented in Fig. 6 for TIB layer 1 and TOB layer 5. The distributions have been fitted with

Table 2: Strip occupancies in the SST subsystems.

	TIB	TOB	TID	TEC
Average number of digis per event	720	1000	300	1700
Number of readout channels / 10^6	1.8	3.1	0.6	3.9
Strip occupancy from digis (%)	0.04	0.03	0.05	0.04
Average number of clusters per event due to noise	1.0	2.0	0.3	3.0

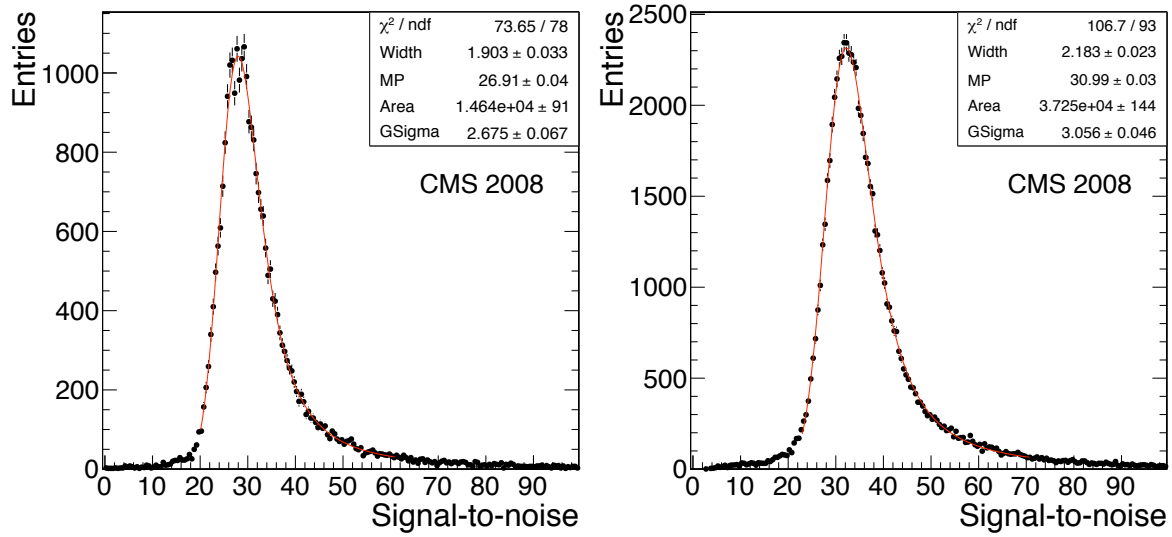

Figure 6: Signal-to-noise ratio distributions of clusters associated to tracks in TIB layer 1 (left) and TOB layer 5 (right).

a Landau function convoluted with a Gaussian function to determine the most probable value for the signal-to-noise ratio. The result is in the range 25-30 for thin modules and 31-36 for thick ones, and within 5% from the expected values. Thick sensors collect about a factor of 5/3 more charge than the thin sensors, but this does not simply scale up the signal-to-noise ratio, as the noise is also larger for thick sensors, because of the longer strips of these modules.

The fit of the signal-to-noise ratio can also be performed on a run-by-run basis; Figure 7 shows the most probable value as a function of run number, allowing to monitor the stability over a period of time. Figure 7 is divided into the three main data-taking periods as discussed in Section 3. It can be seen that in period A the signal-to-noise ratio was lower because muons were out-of-time in the modules not correctly synchronised with the trigger. Temporal variations of 5% arise from residual pedestal and timing mis-calibrations.

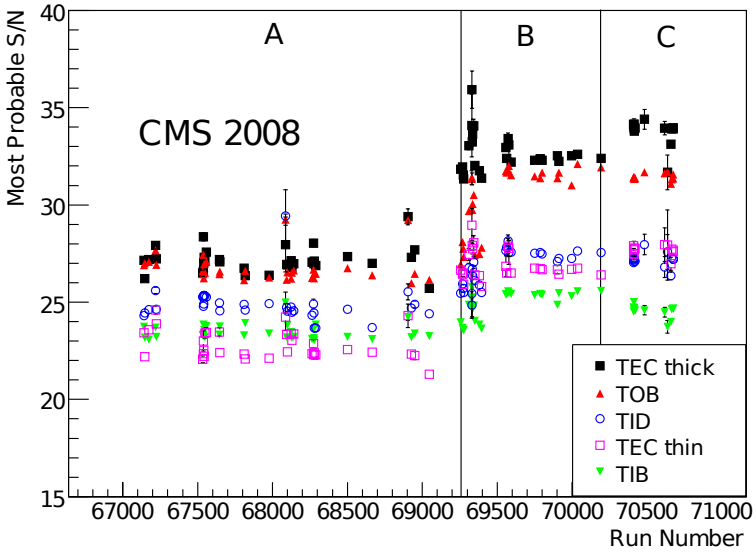

Figure 7: Signal-to-noise ratio versus the run number. The error bars represent the uncertainty associated with the Landau fit described in the text.

4.3 Gain calibration

The charge released in the silicon sensors by the passage of a charged particle is processed by the readout electronics chain described in Section 2.1. The ratio of ADC counts output after FED digitisation to the originally-released charge corresponds to the gain of the electronics chain. Particle identification using energy loss in the silicon detectors [29] is known to be sensitive both to the absolute calibration scale and to gain non-uniformities. It is therefore important that these non-uniformities be corrected for and that the conversion factor between deposited energy and ADC counts is measured precisely.

4.3.1 Inter-calibration of gain

The electronics gain can be made uniform throughout the SST simply by scaling the tick mark heights measured during calibration to an appropriate value. However, this procedure will not take into account gain changes due to temperature variations and non-uniformities in the sensor response to a traversing particle, e.g., because of trigger synchronization, or because the sensor is not fully depleted. For particle identification with energy loss, non-uniformity

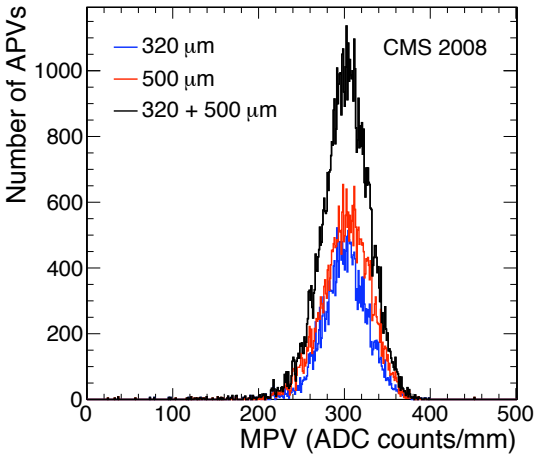

Figure 8: Most probable value of the cluster charge for different thicknesses before gain calibration.

must not exceed 2% [29]. This level of inter-calibration can be achieved only using the signals produced by particles. The path length corrected charge of those clusters associated with tracks was fitted with a separate Landau curve for each APV25 chip. Figure 8 shows the distribution of most probable values for APVs with at least 50 clusters, subdivided by sensor thickness. The spread of these distributions is around 10%.

The most probable value of each distribution is then used to compute the inter-calibration constants by normalising the signal to 300 ADC counts/mm – the value expected for a minimum ionising particle with a calibration of 270 e^-/ADC count (Section 2.5). The inter-calibration constants determined in this manner were used in the final reprocessing of the CRAFT data, resulting in a uniform response.

4.3.2 Absolute calibration using energy deposit information

In addition to the inter-calibration constants, for particle identification using energy loss, the ratio of deposited charge to ADC counts must be measured. The energy loss by particles traversing thin layers of silicon is described by the Landau-Vavilov-Bichsel theory [30]. The most probable energy deposition per unit of length, Δ_p/x, is described by the Bichsel function and depends on both the silicon thickness and the particle momentum. For muons, the function has a minimum at 0.5 GeV/c and then rises to reach a plateau for momenta greater than 10 GeV/c. The absolute gain calibration can be determined by fitting the Bichsel function predictions to the measured Δ_p/x values from the CRAFT data sample.

The quantity Δ_p/x is measured using the charge of clusters associated to tracks as a function of track momentum. The resulting charge distributions are fitted with a Landau convoluted with a Gaussian. Only tracks with at least six hits and χ^2/ndf less than 10 are considered. In addition, only clusters with fewer than four strips are taken into account. This last requirement is imposed in order to avoid mis-reconstructed clusters.

Before the absolute calibration factor can be extracted from the cluster charge data, two corrections must be applied. Firstly, a correction is needed to take into account any charge loss in the zero-suppression process and during clustering. This is determined using Monte Carlo simulations for each subsystem and for both thin and thick sensors in the end caps. Secondly, a correction is needed to handle the imperfect synchronisation between the different subsystems.

Table 3: Absolute gain calibration measured from energy deposit per unit length, Δ_p/x.

Subsystem	TIB	TOB	TEC+ thin	TEC+ thick	TEC- thin	TEC- thick
e^-/ADC count	$262.3^{+2.5}_{-3.5}$	$261.5^{+0.5}_{-1.5}$	273^{+7}_{-9}	270^{+7}_{-9}	264^{+3}_{-4}	261^{+3}_{-4}

Overall, the uncertainty due to these corrections is estimated to be about 1.5%.

Figure 9 shows the most probable value of energy deposition per unit length plotted as a function of the track momentum for both thin and thick sensors. The error bars reflect the uncertainty from the Landau fit, while the bands represent the fully-correlated systematic uncertainties from Monte Carlo corrections. The small dip at 5 GeV/c arises from a temporary problem in the trigger provided by a sector of the muon chambers, because of which this momentum region was contaminated with out-of-time particles. The absolute calibration factor is determined separately for each subsystem and for both thin and thick sensors in TEC+ and TEC-. The resulting values are given in Table 3. If a fit is performed for all SST modules together, the absolute calibration factor is found to be 262$\pm$ 3 e^-/ADC count, which is very similar to the result in the TOB alone, which dominates the data sample. However, thick and thin modules are compatible and overall the result is in agreement with the value of 269 $\pm$ 13 e^-/ADC count obtained from the pulse calibration described in Section 2.5.

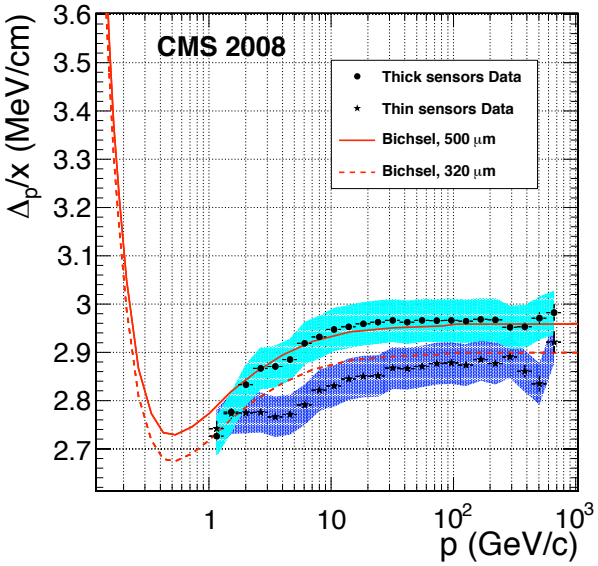

Figure 9: Most probable energy deposit per unit of length Δ_p/x as a function of track momentum, for thin and thick sensors. The shaded bands show the correlated systematic uncertainties on the measurements. The curves are the expectations from the Bichsel function [30] as explained in the text.

4.4 Lorentz angle measurement

In the silicon sensors, the electric field is perpendicular to the strips. For normal incidence particles, typically only one strip is hit and the cluster size increases with the angle of incidence. In the presence of a magnetic field, however, the drift direction is tilted by the Lorentz angle, as illustrated in Fig. 10. This is illustrated, for one module in layer 4 of TOB, in Fig. 11, which shows a profile plot of cluster size versus the tangent of the incidence angle. To extract the

Lorentz angle, this distribution is fitted to the function:

$$f(\theta_t) = \frac{h}{P} \cdot p_1 \cdot |\tan\theta_t - p_0| + p_2$$

where h is the detector thickness, P is the pitch, and p_0, p_1 and p_2 are the fit parameters. The parameter p_0 is, in effect, $\tan\theta_L$, while p_1 represents the slope of the line divided by the ratio of thickness to pitch. The third parameter, p_2, is the average cluster size at the minimum.

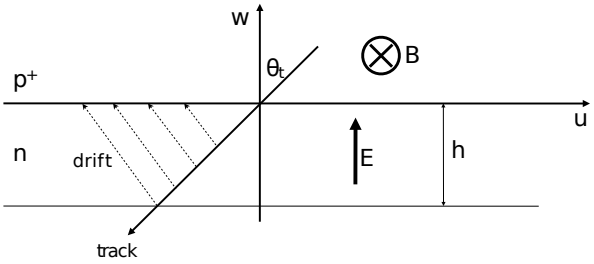

Figure 10: Lorentz drift in the microstrip sensors.

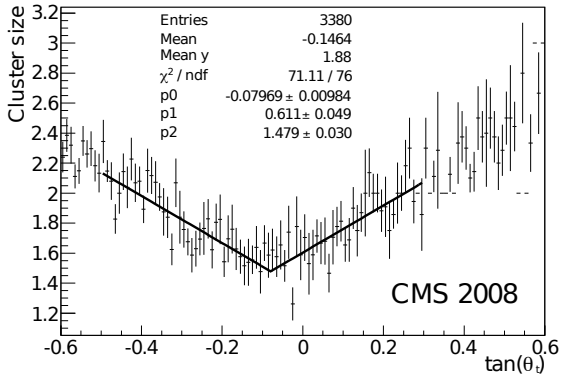

Figure 11: Cluster size versus incident angle in one module of TOB Layer 4.

The Lorentz angle is measured for each individual module. The mean $\tan\theta_L$ is 0.07 in TIB and 0.09 in TOB, with an RMS of 0.02 and 0.01, respectively. A small difference between TIB and TOB is expected because the hole mobility depends on the electric field, and therefore, for the same applied voltage, on the thickness.

The Lorentz angle correction applied to clusters during track reconstruction is relatively small – of the order of 10 μm – but it is still larger than the overall alignment precision [31]. The alignment procedure can therefore provide a useful method of cross-checking the Lorentz angle measurements. In particular, it is useful to compare the residual distributions from data with and without the magnetic field applied. Results from the tracker alignment procedure confirm the measurements presented here [31].

4.5 Hit efficiency

The hit efficiency is the probability to find a cluster in a given silicon sensor that has been traversed by a charged particle. In order to calculate the hit efficiency, track seeding, finding, and reconstruction must be performed. The results presented here have been determined using the Combinatorial Track Finder for cosmic ray muons events (see Section 5.1 for further details),

excluding the clusters in the layer of the SST for which the hit efficiency is to be determined. The efficiency for a given module in this layer is then calculated by finding tracks that pass through that module and determining if a cluster is, in fact, present.

A single run from the CRAFT dataset has been used in order to assure that the number of excluded modules did not change. A very long run was chosen to ensure that the track statistics were sufficient. There were between 16 400 and 104 800 tracks per barrel layer and between 1700 and 6500 per end cap layer. The analysis was limited to events that contained only one track, which was required to have a minimum of eight hits and no more than four missing hits. To ensure that the muon has actually passed through the module under study, the location of the extrapolation of the track trajectory on the module surface was required to be no closer to the sensor edge than five times the position uncertainty of the extrapolated point.

The efficiency results per SST layer are shown in Fig. 12. These measurements, which include all SST modules, are compatible with the expected overall percentage of excluded modules. If the modules that were excluded because of known problems were ignored in the efficiency calculation, the resulting efficiency would be greater than 99% for most layers. No more than about 0.001 of the inefficiency arises from isolated dead strips [7], which are not taken into account in the efficiency calculation for Fig. 12 (right). The rest is attributed to modules that were problematic only for a short period of time and were therefore not identified by the other procedures described in this paper. Subsequent improvements, such as detailed logging of modules affected by temporary power supply problems (HV trips etc.), will improve the bookkeeping of inefficiency for future data-taking.

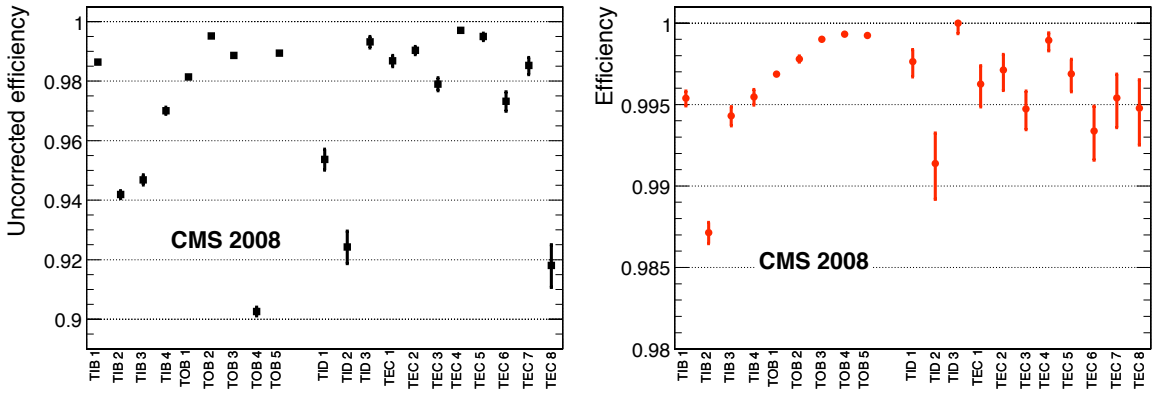

Figure 12: Average module hit efficiency per layer/disk, without any correction for disconnected or otherwise exclude modules (left) and after applying such corrections (right). The efficiency cannot be measured in the outermost layers of TOB (layer 6) or TEC (layer 9) without modifying the track reconstruction algorithm, because the track reconstruction requires the presence of a hit in the outermost layer or disk, depending on the track trajectory.

5 Track Reconstruction

In this section, the performance of the track reconstruction using the full tracker, including the pixel detector, is presented. Details of the commissioning and the performance of the hit reconstruction in the pixel detector can be found elsewhere [3].

5.1 Track reconstruction algorithms

The two main algorithms used to reconstruct tracks from cosmic ray muons in CRAFT data are the Combinatorial Track Finder (CTF) and the Cosmic Track Finder (CosmicTF). The Combinatorial Track Finder is the standard track reconstruction algorithm intended for use with proton-proton collisions and the main focus of the present study; for these runs, it has been specially re-configured to handle the different topology of cosmic muon events. The second algorithm was devised specifically for the reconstruction of single track cosmic ray muon events. Since it is meant as a cross-check of the Combinatorial Track Finder, it has not been tuned to the same level of performance. A full description of these algorithms can be found elsewhere [7].

There have been two significant changes in the Combinatorial Track Finder since its first use in the Slice Test, both relating to the seed finding phase. The Slice Test was performed without the presence of a magnetic field and with only limited angular coverage. Now that the full tracker is available, seed finding in the barrel uses TOB layers only and both hit triplets and pairs are generated. In the end caps, hits in adjacent disks are used to form hit pairs. The presence of the 3.8 T magnetic field means that for hit-triplet seeds, the curvature of the helix yields an initial estimate of the momentum. For hit pairs seeds, an initial estimate of $2\,\mathrm{GeV}/c$ is used, which corresponds to the most probable value. The detector has been aligned with the methods described in Reference [31].

5.2 Track reconstruction results

The number of tracks reconstructed by the two algorithms in the data from Period B, without applying any additional track quality criteria, except those applied during the track reconstruction itself, are 2.2 million using the Combinatorial Track Finder and 2.7 million by the Cosmic Track Finder.

The number of reconstructed tracks per event is shown in Fig. 13, and Fig. 14 shows the distributions of a number of track-related quantities compared between a subset of the data and Monte Carlo simulation. The large number of events without reconstructed tracks is mainly due to muons outside of the fiducial volume for which fewer than five hits are reconstructed in the tracker.

It can be seen that reasonable agreement is found between the data and the Monte Carlo simulation, although there are some discrepancies that require further investigation. These are thought to be due to the reconstruction of showers by the track reconstruction algorithms. The Combinatorial Track Finder is capable of reconstructing more than one track per event, but as it has not been optimised to reconstruct showers, multi-track events tend to contain a number of fake or badly reconstructed tracks. These are mostly low momentum tracks with a small number of hits and large χ^2 values, and the fake rate is estimated to be around 1%. For this reason, only single track events are used in the rest of the results presented in this paper, and the distributions shown in Fig. 14 are only for single track events. Small discrepancies remain for tracks with fewer hits and low momentum. These could be due to detector noise and limitations in the simulation in describing the low momentum range of cosmic ray muons, such as the position of the concrete plug covering the shaft. The simulation assumed that the CMS access shaft was always closed by a thick concrete plug, while, during the data-taking period, it was also opened or half-opened. The absence of the concrete plug causes more low momentum muons to reach the tracker [32]. The noise is responsible for fake hits added to genuine tracks and, occasionally, fake tracks, which contribute to the discrepancies in the χ^2 distribution.

By design the Cosmic Track Finder reconstructs only one track. The difference between the

number of tracks reconstructed by the two algorithms is mainly due to the minimum number of hits required during the pattern recognition phase. In the Combinatorial Track Finder a minimum of five hits are required, while only four are required in the case of the Cosmic Track Finder. It can be seen that a small number of tracks have fewer hits than these minimum requirements. This is due to the fact that hits deemed to be outliers can still be removed in the track fitting phase. It can also be seen from Fig. 14 that there is a significant number of tracks with a high number of hits, indicating that tracks can be followed through the whole tracker and be reconstructed with hits in both the upper and lower hemispheres.

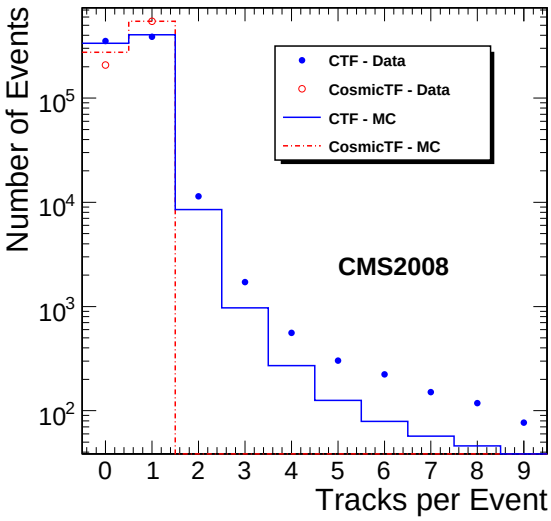

Figure 13: Distribution of the number of tracks reconstructed per event with the two different algorithms. For each algorithm, the total number of simulated Monte Carlo tracks are normalised to the number of observed tracks.

5.3 Track reconstruction efficiency

The track reconstruction efficiency for the two algorithms described above has been measured using two different methods. First, the efficiencies were measured by searching for a reconstructed track and matching it to a muon reconstructed only in the muon chambers. In the second method, the efficiency was measured using data just from the tracker, by reconstructing tracks independently in the upper and lower hemispheres of the tracker. In addition, the likely performance of the Combinatorial Track Finder in proton-proton collisions was estimated by running the algorithm with the appropriate settings and measuring the efficiency by comparing the two segments of traversing cosmic ray muons, i.e. the second method.

5.3.1 Track reconstruction efficiency using muons reconstructed by the muon chambers

In the first method, the track reconstruction efficiency is measured with respect to muons reconstructed using information from the muon chambers, and required to point within the geometrical acceptance of the tracker. This ensures that the muons have been identified independently of the tracker. The muons are first reconstructed by the muon chambers, combining segments of muon tracks reconstructed in the top and bottom hemispheres of the muon detectors in a global fit. These reference muons are required to have at least 52 hits in the muon chambers, which corresponds to having hits in at least five Drift Tube chambers. Combining segments

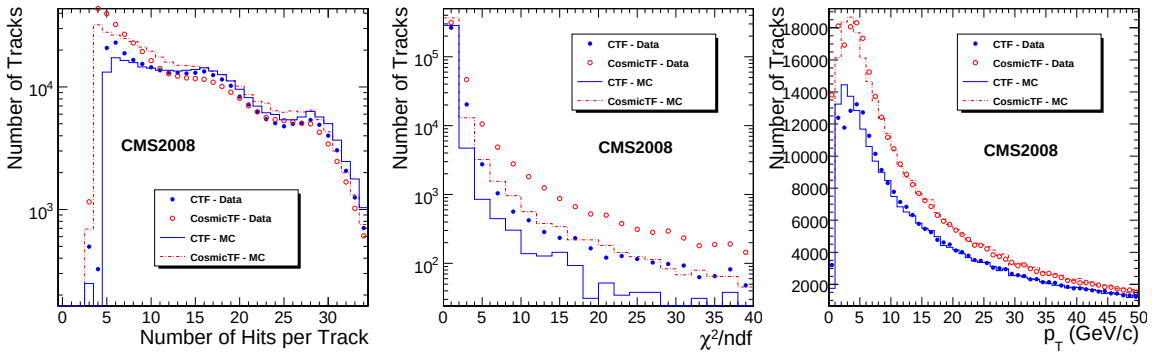

Figure 14: Distributions of several track-related variables for the two different algorithms in single track events: the number of hits per track (left), χ^2/ndf (middle) and the transverse momentum (right). Note that for the χ^2/ndf distribution, a log-scale is used for the y-axis. For each algorithm, the total number of simulated Monte Carlo tracks are normalised to the number of observed tracks.

from the two hemispheres removes muons which are absorbed by the CMS steel yoke before reaching the tracker. It also improves the track direction reconstruction, which is needed for the propagation through the detector.

The efficiency is estimated with respect to reference muons with a topology similar to that expected in proton-proton collisions. This is achieved by requiring that the point of closest approach of the extrapolated muon to the centre of the detector is less than 30 cm in both the transverse and longitudinal directions. The absolute value of the pseudorapidity, $|\eta|$, is required to be less than 1 and the azimuthal angle is required to be in the range $0.5 < |\phi| < 2.5$, effectively restricting the tracks to the barrel. These cuts also ensure that the tracks cross most of the layers of the tracker and cross most modules perpendicularly. The efficiency is then measured by searching for a corresponding track reconstructed in the tracker.

The efficiencies measured in the data and in the Monte Carlo simulation are compared in Fig. 15 (left) and summarised in Table 4. The efficiencies are higher than 99% for both data and Monte Carlo simulation and for the two tracking algorithms. The difference between data and Monte Carlo observed around 20 GeV/c for the Cosmic Track Finder, while statistically significant, is small and has not been pursued further, since this algorithm will not be used in proton-proton collisions. The overall differences between data and Monte Carlo simulation are found to be smaller than 0.5%.

Table 4: Track reconstruction efficiencies for the two algorithms in Data and in Monte Carlo simulation, measured with the muon-matching method.

	CTF		CosmicTF	
	Data	MC	Data	MC
Efficiency (%)	99.78 ± 0.02	99.88 ± 0.01	99.47 ± 0.04	99.72 ± 0.01

5.3.2 Track reconstruction efficiency using tracker data only

In the second method, the efficiency is measured using data from the tracker; no muon chamber information is included. This method has been used in previous cosmic ray muon data-taking

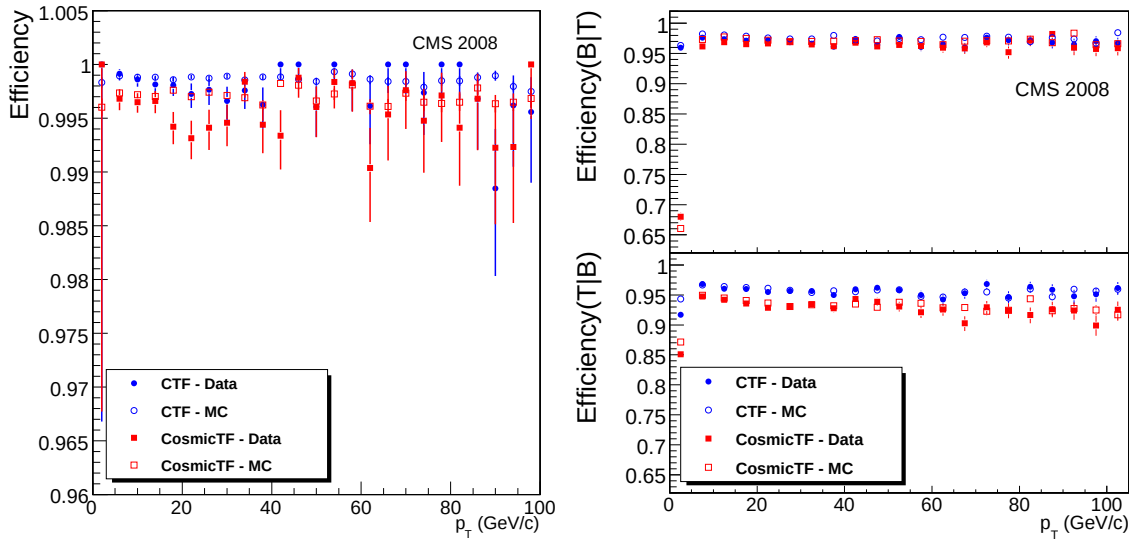

Figure 15: Track reconstruction efficiency as a function of the measured transverse momentum of the reference track, as measured with the track-muon matching method (left) and the Top/Bottom comparison method (right).

exercises, when the efficiency was evaluated using track segments reconstructed separately in the TIB and TOB [7]. As cosmic ray muons pass through the tracker from top to bottom, the tracker was divided into two hemispheres along the $y = 0$ horizontal plane for this study. The tracks were reconstructed independently in the two hemispheres. Tracks reconstructed in the upper hemisphere are referred to as *top tracks* and those reconstructed in the lower hemisphere as *bottom tracks*. Tracks in one hemisphere are used as references to measure the efficiency in the other hemisphere. Two such measurements are performed: $\epsilon(T|B)$, where, given a bottom track, a matching top track is sought and vice versa ($\epsilon(B|T)$). The matching is performed by requiring that the two opposite-half tracks have pseudorapidities that satisfy $|\Delta\eta| < 0.5$.

Only events containing a single track with a topology similar to that expected in proton-proton collisions are analysed and the same track requirements that were applied in Section 5.3.1 are used. To reconstruct the two track legs independently, only seeds with hits in the top or bottom hemisphere are selected and, before the final track fit, the hits in the other hemisphere are removed from the track. After track segment reconstruction, a track is only retained for further analysis if it contains at least 7 hits and satisfies the requirement $\chi^2/\mathrm{ndf} > 10$. Furthermore, to ensure that a matching track can be reconstructed, the extrapolation of the reference track into the other hemisphere is required to cross at least five layers.

The efficiencies measured using this method are shown in Fig. 15 (right) and Table 5. The difference seen for low momentum tracks for the Cosmic Track Finder is small, and has not been pursued further. The lower efficiency for top tracks is primarily caused by a large inactive area in the upper half of TOB layer 4, which would otherwise be used to build track seeds. This will not be an issue for the track reconstruction that will be used in proton-proton collisions as in this case, tracks are seeded principally in the pixel detector with the tracking then proceeding towards the outer layers of the SST. The efficiencies measured in the Monte Carlo simulation are consistent with those measured in the data to within 1%.

Table 5: Overall track reconstruction efficiency measured with the top/bottom comparison method.

	CTF		CosmicTF	
	Data	MC	Data	MC
$\epsilon(B\|T)$ (%)	97.03±0.07	97.56±0.04	94.01±0.10	93.41±0.06
$\epsilon(T\|B)$ (%)	95.61±0.08	95.79±0.05	92.65±0.11	93.19±0.07

5.3.3 Inside-out tracking method

Finally, to evaluate the algorithm that will be used during proton-proton collisions, the efficiency of the Combinatorial Track Finder with the appropriate settings is measured. The reconstruction process [23] starts in the centre of the tracker and proceeds to the outside, using seeds constructed primarily in the pixel detector. The default Combinatorial Track Finder is optimised to reconstruct tracks that originate near the interaction point. By contrast, very few cosmic ray muons will pass through this region. In order to take this into account, only tracks for which the point of closest approach to the centre of the detector is less than 4 cm in the transverse direction and 25 cm in the longitudinal direction are used, effectively crossing the three barrel layers of the pixel detector.

The tracks are reconstructed from a seed made with hit pairs from any combination of the innermost three layers of the SST; the nominal beam spot is used as an additional constraint in the transverse plane to provide the initial estimate of the track parameters. This is a legitimate approximation as long as the transverse impact parameter of the tracks is much smaller than the radius of the innermost detector layer used. Hits in the silicon pixel detector are not used in this analysis in the seed finding phase, as this imposes too strong a constraint on the tracks to come from the nominal beam spot. They are, however, identified in the pattern recognition phase and added to the track.

The reconstruction efficiencies are estimated with respect to a reference track in one hemisphere of the tracker. A compatible seed and track is sought in the other hemisphere within a cone of radius $\Delta R < 1.0$ (where $\Delta R = \sqrt{\Delta\eta^2 + \Delta\phi^2}$) opposite to the reference track. The cone size is kept very large compared to the angular resolution so that the matching procedure cannot bias the efficiency measurements. To avoid multi-track events, a track is not used as a reference if there is another track in the same hemisphere or within the matching cone. Fake tracks created by noisy hits are rejected by requiring that the reference tracks have at least 10 hits.

The efficiencies measured using this method are shown in Fig. 16 and in Table 6. These efficiencies can be further divided into a *seed finding* efficiency, which is the efficiency of building a seed for a given reference track, and a *pattern recognition* efficiency, which is the efficiency of reconstructing a track once a seed has been found. Inefficiencies affecting only a few detector channels have not been taken into account when calculating the overall efficiency from the data. The efficiencies measured in the Monte Carlo simulation match those measured in the data to within 1%.

5.3.4 Summary of the track efficiency measurements

The three methods of efficiency calculation presented in this section yield consistent results and indicate that a high track reconstruction efficiency is attained for vertical tracks passing close to the nominal beam line, which is the topology most similar to the tracks from proton-proton collisions. Although the results are similar, some small differences were observed. The main

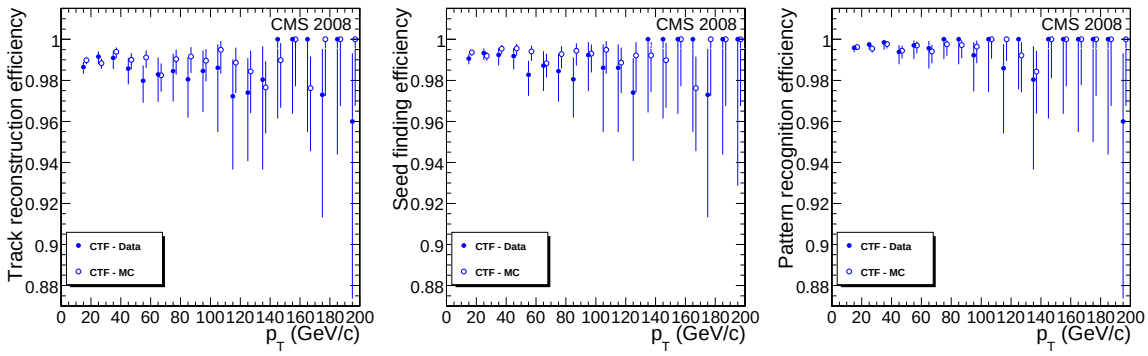

Figure 16: Track reconstruction efficiency (left), seed finding efficiency (middle), and pattern recognition efficiency (right) as a function of the measured transverse momentum of the reference track for inside-out tracking method. Note that the Monte Carlo points are shifted by 2GeV/c so as to allow the uncertainties to be seen.

Table 6: Reconstruction efficiency of the Inside-out tracking method.

	Data	MC
Seed finding efficiency (%)	99.17 ± 0.12	99.30 ± 0.08
Pattern recognition efficiency (%)	99.79 ± 0.06	99.64 ± 0.05
Track reconstruction efficiency (%)	98.96 ± 0.13	98.94 ± 0.09

difference between the efficiencies determined by the first and second methods arises from the fact that tracks are sought in only one half of the detector in the second method, while in the first method, tracks may be found from seeds produced in both halves of the tracker.

The Combinatorial Track Finder algorithm has been fully tested and is well understood, yielding a high quality performance. The Cosmic Track Finder algorithm, while not tuned to the level of the Combinatorial Track Finder, also achieves good performance and provides a fundamental cross-check. The measurements of the "Inside-out tracking method" give confidence that the track reconstruction will perform well in proton-proton collisions. Finally, the efficiencies measured in the Monte Carlo simulation agree very well with those measured in the data once the known detector inefficiencies are accounted for in the simulation. This indicates that the tracker and the reconstruction algorithms are well understood.

5.4 Track parameter resolution

The track reconstruction can be further validated using the CRAFT data sample by splitting the tracks into two separate parts. A measure of the resolution of the track parameters can be determined by comparing the two legs of the split tracks. To perform this study, tracks are split at the point of closest approach to the nominal beam-line. The top and bottom legs are treated as two independent tracks and re-fitted accordingly. The track parameters are then propagated to their respective points of closest approach to the beam-line. This method has been tested using Monte Carlo simulation and found to work well.

For the purposes of this study, only events in which the Combinatorial Track Finder reconstructed a single track whose point of closest approach to the beam-line is inside the volume of the pixel barrel are considered. The transverse momentum of the track must be greater than

Table 7: Standard deviation, mean, and 95% coverage of the residual and pull distributions of the track parameters. The units indicated pertain only to the residual distributions.

Track parameter	Residual distributions			Pull distributions		
	Std. Dev.	Mean	95% Cov.	Std. Dev.	Mean	95% Cov.
p_T (GeV/c)	0.083	0.000	1.92	0.99	0.01	2.1
Inverse p_T (GeV^{-1}c)	0.00035	0.00003	0.00213	0.99	-0.01	2.1
ϕ (mrad)	0.19	0.001	0.87	1.08	-0.02	2.4
θ (mrad)	0.40	0.003	1.11	0.93	-0.01	2.1
d_{xy} (μm)	22	0.30	61	1.22	0.00	2.9
d_z (μm)	39	0.28	94	0.94	-0.01	2.1

4 GeV/c and its χ^2 must satisfy the requirement $\chi^2/\text{ndf} < 100$. In addition, the track must contain a minimum of 10 hits, with at least two hits being on double-sided strip modules. There must also be six hits in the pixel barrel subsystem. After splitting, each track segment is required to have at least six hits, three of which must be in the pixel barrel.

The results of this analysis are summarised in Table 7, while the distributions of the residuals and pulls of the inverse transverse momentum and the azimuthal (ϕ) and polar (θ) angles are shown in Fig. 17. The corresponding distributions for the transverse (d_{xy}) and longitudinal (d_z) impact parameters can be found elsewhere [3]. For each track parameter, the residuals are defined as $\delta x = (x_1 - x_2)/\sqrt{2}$. The factor of $\sqrt{2}$ is needed to account for the fact that the two legs are statistically independent. The standardised residuals (or pulls) are defined by $\widetilde{\delta x} = (x_1 - x_2)/\sqrt{\sigma_{x1}^2 + \sigma_{x2}^2}$. In Table 7 the mean and standard deviation (referred to as the *resolution*) of a Gaussian fitted to the peak of the distributions are given. In order to get an estimate of the tails of the distributions, the half-widths of the symmetric intervals covering 95% of the distribution (also known as the *95% coverage*), which, in the case of a Gaussian distribution, correspond to twice the standard deviation, are also given in Table 7.

The same quantities are used to characterise the pull distributions. In this case, the standard deviations of the fitted Gaussians are taken as the pull values. It can be seen that the resolution of the angles and the impact parameters are well described by a Gaussian. The resolution as a function of the momentum has been presented elsewhere [31].

5.5 Hit resolution

The hit resolution has been studied by measuring the track residuals, which are defined as the difference between the hit position and the track position. The track is deliberately reconstructed excluding the hit under study in order to avoid bias. The uncertainty relating to the track position is much larger than the inherent hit resolution, so a single track residual is not sensitive to the resolution. However, the track position difference between two nearby modules can be measured with much greater precision. A technique using tracks passing through overlapping modules from the same tracker layer is employed to compare the difference in residual values for the two measurements in the overlapping modules [7]. The difference in hit positions, Δx_{hit}, is compared to the difference in the predicted positions, Δx_{pred}, and the width of the resulting distribution arises from the hit resolution and the uncertainty from the tracking predictions. The hit resolution can therefore be determined by subtracting the uncertainty from the tracking prediction. This overlap technique also serves to reduce the uncertainty arising from multiple scattering, by limiting the track extrapolation to short distances. Any uncertainty from translational misalignment between the modules is also avoided by fitting a

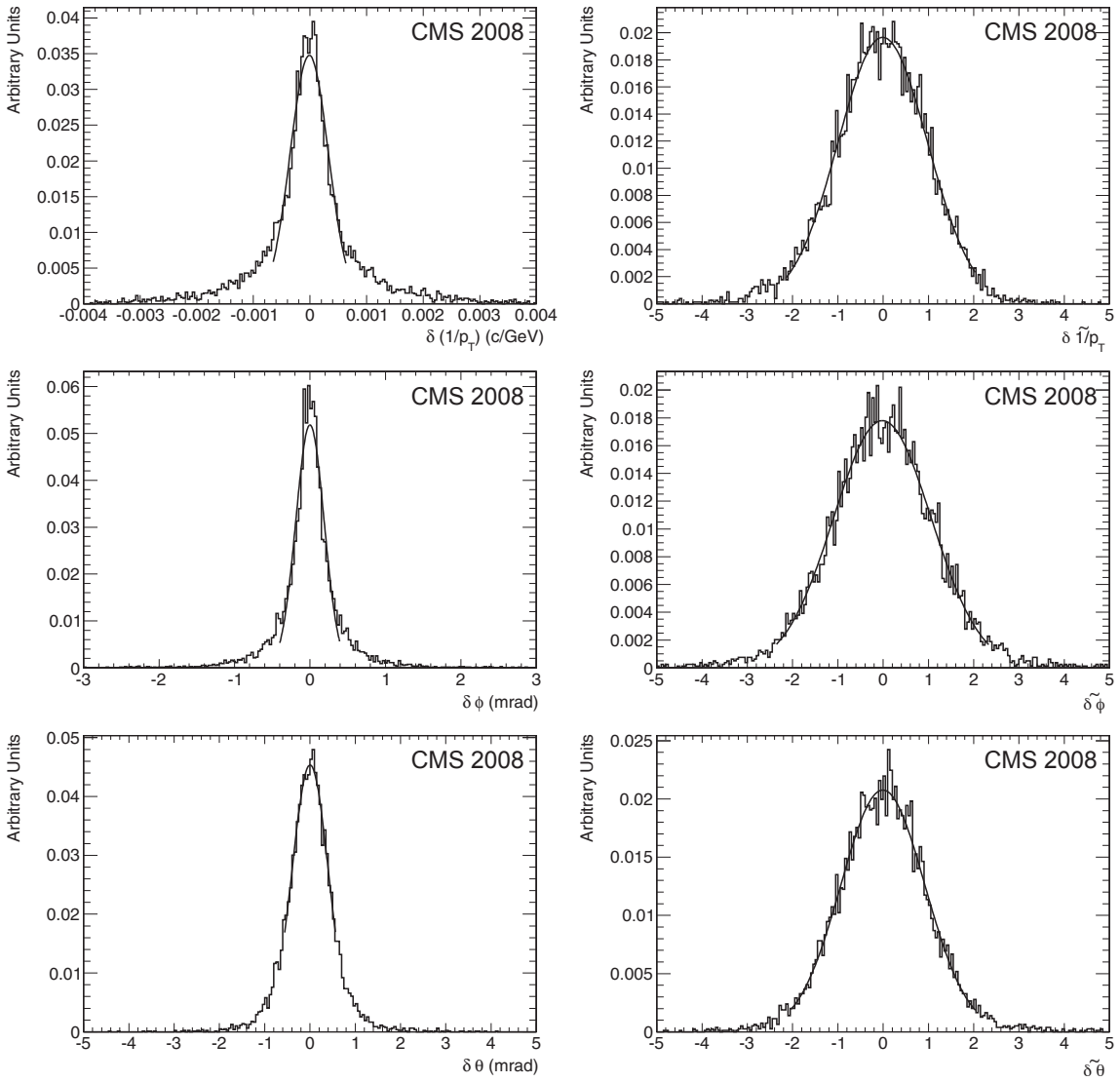

Figure 17: Residual distribution (left) and pull distribution (right) of the inverse transverse momentum $1/p_{\mathrm{T}}$ (top), azimuthal ϕ (middle), and polar θ angle (bottom).

Gaussian to the distribution of the differences between the residuals.

For the purposes of this study, only events in which the Combinatorial Track Finder reconstructed a single track are used, and only overlaps from barrel modules for which the residual rotational misalignment is less than $5\,\mu$m are analysed. The χ^2 probability of the track is required to exceed 0.1% and the tracks must be reconstructed with at least 6 hits. In addition, the track momenta are required to be greater than $20\,\mathrm{GeV}/c$, ensuring that the uncertainty arising from multiple scattering is reduced to less than $3\,\mu$m. Remaining uncertainties from multiple scattering and rotational misalignment between the overlapping modules are included as systematic uncertainties in the measurement.

The distribution of the differences between the residuals is fitted, with the width containing contributions from the hit resolutions and the uncertainty from the tracking predictions. The latter is subtracted out in quadrature to leave the resolution on the difference of the hit positions

Table 8: Hit resolution measured on CRAFT data and predicted by the model in the Monte Carlo simulation, for the different local track angles. All values are in microns.

Sensor	Pitch (μm)	Resolution (μm)	Track angle			
			$0^\circ - 10^\circ$	$10^\circ - 20^\circ$	$20^\circ - 30^\circ$	$30^\circ - 40^\circ$
TIB 1-2	80	Measurement	17.2 ± 1.9	14.3 ± 2.3	17.4 ± 3.2	25.7 ± 6.0
		MC Prediction	16.6 ± 0.5	11.8 ± 0.5	12.4 ± 0.6	17.9 ± 1.5
TIB 3-4	120	Measurement	27.7 ± 3.6	18.5 ± 3.1	16.1 ± 3.1	24.1 ± 6.7
		MC Prediction	26.8 ± 0.7	19.4 ± 0.8	17.2 ± 0.3	21.4 ± 2.0
TOB 1-4	183	Measurement	39.6 ± 5.7	28.0 ± 5.8	24.8 ± 6.5	32.8 ± 8.3
		MC Prediction	39.4 ± 1.3	27.8 ± 1.2	26.5 ± 0.3	32.5 ± 2.1
TOB 5-6	122	Measurement	23.2 ± 3.6	19.5 ± 3.6	20.9 ± 6.1	29.3 ± 9.7
		MC Prediction	23.8 ± 0.9	18.0 ± 0.5	19.2 ± 1.2	25.4 ± 1.6

between the two modules. As the two overlapping modules are expected to have the same resolution, the resolution of a single sensor is determined by dividing by $\sqrt{2}$.

The sensor resolution is known to depend strongly on the angle of the track and the pitch of the sensor. The results are therefore determined separately for different sensor pitches and in 10 degree intervals for the track incidence angle. The results are shown in Table 8, where they are compared to the predictions from Monte Carlo simulation. The agreement between the data and the predictions is very good for normally incident tracks, but suggests that the simulation may underestimate the resolution for larger track angles, as can be seen in the first two layers of TIB. The resolutions vary from 20 to 56 μm for the position difference, which corresponds to a variation between 14 and 40 μm in the single sensor resolution.

6 Summary

The Cosmic Run At Four Tesla has been an important experience for commissioning the tracker.

The control and readout systems were successfully commissioned, synchronised to the Level-1 Trigger, and operated in global runs with all the other sub-detectors of the CMS experiment. The total number of modules used corresponds to 98.0% of the total system.

About 15 million events with a muon in the tracker were collected. The hit and track reconstruction are seen to have an excellent performance and the Combinatorial Track Finder, which will be used in proton-proton collisions as the default reconstruction algorithm, was tested successfully. The signal-to-noise performance is in the range 25-30 for thin modules and 31-36 for thick ones. The efficiency of hit reconstruction is above 99.5%. In addition, with the collected data sample, it has been possible to calibrate the measurement of energy loss in silicon and to measure the Lorentz angle.

The track reconstruction efficiency has been measured with two different methods: one using only muons reconstructed in the muon chambers and one using only data from the tracker. The reconstruction efficiency in data was found to be high and well described by the Monte Carlo simulation. For tracks passing close to the centre of the detector and having a direction close to the vertical axis, the reconstruction efficiency was found to be higher than 99%. The resolution on hit position and track parameters was also consistent with expectations from Monte Carlo simulation.

CRAFT demonstrated the successful operation of the tracker integrated with the other CMS

subsystems. It was an important milestone towards final commissioning with colliding beam data.

Acknowledgments

We thank the technical and administrative staff at CERN and other CMS Institutes, and acknowledge support from: FMSR (Austria); FNRS and FWO (Belgium); CNPq, CAPES, FAPERJ, and FAPESP (Brazil); MES (Bulgaria); CERN; CAS, MoST, and NSFC (China); COLCIENCIAS (Colombia); MSES (Croatia); RPF (Cyprus); Academy of Sciences and NICPB (Estonia); Academy of Finland, ME, and HIP (Finland); CEA and CNRS/IN2P3 (France); BMBF, DFG, and HGF (Germany); GSRT (Greece); OTKA and NKTH (Hungary); DAE and DST (India); IPM (Iran); SFI (Ireland); INFN (Italy); NRF (Korea); LAS (Lithuania); CINVESTAV, CONACYT, SEP, and UASLP-FAI (Mexico); PAEC (Pakistan); SCSR (Poland); FCT (Portugal); JINR (Armenia, Belarus, Georgia, Ukraine, Uzbekistan); MST and MAE (Russia); MSTDS (Serbia); MICINN and CPAN (Spain); Swiss Funding Agencies (Switzerland); NSC (Taipei); TUBITAK and TAEK (Turkey); STFC (United Kingdom); DOE and NSF (USA). Individuals have received support from the Marie-Curie IEF program (European Union); the Leventis Foundation; the A. P. Sloan Foundation; and the Alexander von Humboldt Foundation.

References

[1] CMS Collaboration, "The CMS experiment at the CERN LHC", *JINST* **3** (2008) S08004. doi:10.1088/1748-0221/3/08/S08004.

[2] L. Evans, (ed.) and P. Bryant, (ed.), "LHC Machine", *JINST* **3** (2008) S08001. doi:10.1088/1748-0221/3/08/S08001.

[3] CMS Collaboration, "The CMS Pixel Detector Operation and Performance at the Cosmic Run at Four Tesla", CMS-CFT-09-001. To be submitted to JINST.

[4] L. Borrello et al., "Sensor Design for the CMS Silicon Strip Tracker", *CMS Note* **2003/020** (2003).

[5] W. Adam et al., "The CMS tracker operation and performance at the Magnet Test and Cosmic Challenge", *JINST* **3** (2008) P07006. doi:10.1088/1748-0221/3/07/P07006.

[6] W. Adam et al., "Performance studies of the CMS Strip Tracker before installation", *JINST* **4** (2009) P06009. doi:10.1088/1748-0221/4/06/P06009.

[7] W. Adam et al., "Stand-alone Cosmic Muon Reconstruction Before Installation of the CMS Silicon Strip Tracker", *JINST* **4** (2009) P05004. doi:10.1088/1748-0221/4/05/P05004.

[8] CMS Collaboration, "The CMS Cosmic Run at Four Tesla", CMS-CFT-09-008. To be submitted to JINST.

[9] CMS Collaboration, "The Tracker Project: Technical design report", *CERN-LHCC* **1998-006** (1998).

[10] M. Raymond et al., "The CMS Tracker APV25 0.25 μm CMOS Readout Chip", *Proceedings of the 6th workshop on electronics for LHC experiments, Krakow* (2000) 130.

[11] J. Troska et al., "Optical readout and control systems for the CMS tracker", *IEEE Trans. Nucl. Sci.* **50** (2003) 1067–1072. doi:10.1109/TNS.2003.815124.

[12] C. Foudas et al., "The CMS tracker readout front end driver", *IEEE Trans. Nucl. Sci.* **52** (2005) 2836–2840, arXiv:physics/0510229. doi:10.1109/TNS.2005.860173.

[13] F. Drouhin et al., "The CERN CMS tracker control system ", *Nuclear Science Symposium Conference Record, IEEE* **2** (2004) 1196.

[14] K. Kloukinas et al., "FEC-CCS: A common front-end controller card for the CMS detector electronics", *Proceedings of the 12th Workshop on Electronics for LHC and Future Experiments (LECC 2006), Valencia* (2006) 179.

[15] C. Paillard, C. Ljuslin, and A. Marchioro, "The CCU25: A network oriented communication and control unit integrated circuit in a 0.25-mu-m CMOS technology", *Proceedings of the 8th Workshop on Electronics for LHC Experiments, Colmar* (2002) 174.

[16] S. Gadomski et al., "The Deconvolution method of fast pulse shaping at hadron colliders", *Nucl. Instrum. Meth.* **A320** (1992) 217–227. doi:10.1016/0168-9002(92)90779-4.

[17] S. Paoletti, "The implementation of the power supply system of the CMS silicon strip tracker", *in 10th Workshop on Electronics for LHC and future experiments* (2004) CERN-2004-010, CERN-LHCC-2004-030.

[18] G. Magazzu, A. Marchioro, and P. Moreira, "The detector control unit: An ASIC for the monitoring of the CMS silicon tracker", *IEEE Trans. Nucl. Sci.* **51** (2004) 1333–1336. doi:10.1109/TNS.2004.832925.

[19] G. Cervelli, A. Marchioro, P. Moreira et al., "A radiation tolerant laser driver array for optical transmission in the LHC experiments", *Proceedings of the 7th Workshop on Electronics for LHC Experiments, Stockholm* (2001).

[20] P. Placidi, A. Marchioro, P. Moreira et al., "A 40-MHz clock and trigger recovery circuit for the CMS tracker fabricated in a 0.25-mu-m CMOS technology and using a self calibration technique", *Proceedings of the 5th Workshop on Electronics for the LHC Experiments, Snowmass, Colorado* (1999) 469.

[21] C. Delaere et al., "Procedure for the fine delay adjustment of the CMS tracker,", *CMS Note* **2008/007** (2008).

[22] CMS Collaboration, "Performance of the CMS Drift-Tube Local Trigger with Cosmic Rays", CFT-09-022. To be submitted to JINST.

[23] CMS Collaboration, "CMS physics: Technical design report", *CERN-LHCC* **2006-001** (2006).

[24] CMS Collaboration, "CMS Data Processing Workflows During an Extended Cosmic Ray Run", CMS-CFT-09-007. To be submitted to JINST.

[25] A. Afaq et al., "The CMS dataset bookkeeping service", *J. Phys. Conf. Ser.* **119** (2008) 072001. doi:10.1088/1742-6596/119/7/072001.

[26] CMS Collaboration, "Performance of the CMS Level-1 Trigger during Commissioning with Cosmic Rays", CMS-CFT-09-013. To be submitted to JINST.

[27] P. Biallass, T. Hebbeker, and K. Höpfner, "Simulation of Cosmic Muons and Comparison with Data from Cosmic Challenge using Drift Tube Chambers", *CMS Note* **2007/024** (2007).

[28] P. Biallass and T. Hebbeker, "Parameterisation of the Cosmic Muon Flux for the Generator CMSCGEN", arXiv:0907.5514.

[29] A. Giammanco, "Particle Identification with Energy Loss in the CMS Silicon Strip Tracker", *CMS Note* **2008/005** (2008).

[30] H. Bichsel, "Straggling in thin silicon detectors", *Rev. Mod. Phys.* **60** (1988) 663–699. doi:10.1103/RevModPhys.60.663.

[31] CMS Collaboration, "Alignment of the CMS inner tracking system with cosmic ray particles", CMS-CFT-09-003. To be submitted to JINST.

[32] CMS Collaboration, "Performance of CMS Muon Reconstruction in Cosmic-Ray Events", CFT-09-014. To be submitted to JINST.

A The CMS Collaboration

Yerevan Physics Institute, Yerevan, Armenia
S. Chatrchyan, V. Khachatryan, A.M. Sirunyan

Institut für Hochenergiephysik der OeAW, Wien, Austria
W. Adam, B. Arnold, H. Bergauer, T. Bergauer, M. Dragicevic, M. Eichberger, J. Erö, M. Friedl, R. Frühwirth, V.M. Ghete, J. Hammer[1], S. Hänsel, M. Hoch, N. Hörmann, J. Hrubec, M. Jeitler, G. Kasieczka, K. Kastner, M. Krammer, D. Liko, I. Magrans de Abril, I. Mikulec, F. Mittermayr, B. Neuherz, M. Oberegger, M. Padrta, M. Pernicka, H. Rohringer, S. Schmid, R. Schöfbeck, T. Schreiner, R. Stark, H. Steininger, J. Strauss, A. Taurok, F. Teischinger, T. Themel, D. Uhl, P. Wagner, W. Waltenberger, G. Walzel, E. Widl, C.-E. Wulz

National Centre for Particle and High Energy Physics, Minsk, Belarus
V. Chekhovsky, O. Dvornikov, I. Emeliantchik, A. Litomin, V. Makarenko, I. Marfin, V. Mossolov, N. Shumeiko, A. Solin, R. Stefanovitch, J. Suarez Gonzalez, A. Tikhonov

Research Institute for Nuclear Problems, Minsk, Belarus
A. Fedorov, A. Karneyeu, M. Korzhik, V. Panov, R. Zuyeuski

Research Institute of Applied Physical Problems, Minsk, Belarus
P. Kuchinsky

Universiteit Antwerpen, Antwerpen, Belgium
W. Beaumont, L. Benucci, M. Cardaci, E.A. De Wolf, E. Delmeire, D. Druzhkin, M. Hashemi, X. Janssen, T. Maes, L. Mucibello, S. Ochesanu, R. Rougny, M. Selvaggi, H. Van Haevermaet, P. Van Mechelen, N. Van Remortel

Vrije Universiteit Brussel, Brussel, Belgium
V. Adler, S. Beauceron, S. Blyweert, J. D'Hondt, S. De Weirdt, O. Devroede, J. Heyninck, A. Kalogeropoulos, J. Maes, M. Maes, M.U. Mozer, S. Tavernier, W. Van Doninck[1], P. Van Mulders, I. Villella

Université Libre de Bruxelles, Bruxelles, Belgium
O. Bouhali, E.C. Chabert, O. Charaf, B. Clerbaux, G. De Lentdecker, V. Dero, S. Elgammal, A.P.R. Gay, G.H. Hammad, P.E. Marage, S. Rugovac, C. Vander Velde, P. Vanlaer, J. Wickens

Ghent University, Ghent, Belgium
M. Grunewald, B. Klein, A. Marinov, D. Ryckbosch, F. Thyssen, M. Tytgat, L. Vanelderen, P. Verwilligen

Université Catholique de Louvain, Louvain-la-Neuve, Belgium
S. Basegmez, G. Bruno, J. Caudron, C. Delaere, P. Demin, D. Favart, A. Giammanco, G. Grégoire, V. Lemaitre, O. Militaru, S. Ovyn, K. Piotrzkowski[1], L. Quertenmont, N. Schul

Université de Mons, Mons, Belgium
N. Beliy, E. Daubie

Centro Brasileiro de Pesquisas Fisicas, Rio de Janeiro, Brazil
G.A. Alves, M.E. Pol, M.H.G. Souza

Universidade do Estado do Rio de Janeiro, Rio de Janeiro, Brazil
W. Carvalho, D. De Jesus Damiao, C. De Oliveira Martins, S. Fonseca De Souza, L. Mundim, V. Oguri, A. Santoro, S.M. Silva Do Amaral, A. Sznajder

Instituto de Fisica Teorica, Universidade Estadual Paulista, Sao Paulo, Brazil

T.R. Fernandez Perez Tomei, M.A. Ferreira Dias, E. M. Gregores[2], S.F. Novaes

Institute for Nuclear Research and Nuclear Energy, Sofia, Bulgaria
K. Abadjiev[1], T. Anguelov, J. Damgov, N. Darmenov[1], L. Dimitrov, V. Genchev[1], P. Iaydjiev, S. Piperov, S. Stoykova, G. Sultanov, R. Trayanov, I. Vankov

University of Sofia, Sofia, Bulgaria
A. Dimitrov, M. Dyulendarova, V. Kozhuharov, L. Litov, E. Marinova, M. Mateev, B. Pavlov, P. Petkov, Z. Toteva[1]

Institute of High Energy Physics, Beijing, China
G.M. Chen, H.S. Chen, W. Guan, C.H. Jiang, D. Liang, B. Liu, X. Meng, J. Tao, J. Wang, Z. Wang, Z. Xue, Z. Zhang

State Key Lab. of Nucl. Phys. and Tech., Peking University, Beijing, China
Y. Ban, J. Cai, Y. Ge, S. Guo, Z. Hu, Y. Mao, S.J. Qian, H. Teng, B. Zhu

Universidad de Los Andes, Bogota, Colombia
C. Avila, M. Baquero Ruiz, C.A. Carrillo Montoya, A. Gomez, B. Gomez Moreno, A.A. Ocampo Rios, A.F. Osorio Oliveros, D. Reyes Romero, J.C. Sanabria

Technical University of Split, Split, Croatia
N. Godinovic, K. Lelas, R. Plestina, D. Polic, I. Puljak

University of Split, Split, Croatia
Z. Antunovic, M. Dzelalija

Institute Rudjer Boskovic, Zagreb, Croatia
V. Brigljevic, S. Duric, K. Kadija, S. Morovic

University of Cyprus, Nicosia, Cyprus
R. Fereos, M. Galanti, J. Mousa, A. Papadakis, F. Ptochos, P.A. Razis, D. Tsiakkouri, Z. Zinonos

National Institute of Chemical Physics and Biophysics, Tallinn, Estonia
A. Hektor, M. Kadastik, K. Kannike, M. Müntel, M. Raidal, L. Rebane

Helsinki Institute of Physics, Helsinki, Finland
E. Anttila, S. Czellar, J. Härkönen, A. Heikkinen, V. Karimäki, R. Kinnunen, J. Klem, M.J. Kortelainen, T. Lampén, K. Lassila-Perini, S. Lehti, T. Lindén, P. Luukka, T. Mäenpää, J. Nysten, E. Tuominen, J. Tuominiemi, D. Ungaro, L. Wendland

Lappeenranta University of Technology, Lappeenranta, Finland
K. Banzuzi, A. Korpela, T. Tuuva

Laboratoire d'Annecy-le-Vieux de Physique des Particules, IN2P3-CNRS, Annecy-le-Vieux, France
P. Nedelec, D. Sillou

DSM/IRFU, CEA/Saclay, Gif-sur-Yvette, France
M. Besancon, R. Chipaux, M. Dejardin, D. Denegri, J. Descamps, B. Fabbro, J.L. Faure, F. Ferri, S. Ganjour, F.X. Gentit, A. Givernaud, P. Gras, G. Hamel de Monchenault, P. Jarry, M.C. Lemaire, E. Locci, J. Malcles, M. Marionneau, L. Millischer, J. Rander, A. Rosowsky, D. Rousseau, M. Titov, P. Verrecchia

Laboratoire Leprince-Ringuet, Ecole Polytechnique, IN2P3-CNRS, Palaiseau, France
S. Baffioni, L. Bianchini, M. Bluj[3], P. Busson, C. Charlot, L. Dobrzynski, R. Granier de Cassagnac, M. Haguenauer, P. Miné, P. Paganini, Y. Sirois, C. Thiebaux, A. Zabi

Institut Pluridisciplinaire Hubert Curien, Université de Strasbourg, Université de Haute Alsace Mulhouse, CNRS/IN2P3, Strasbourg, France
J.-L. Agram[4], A. Besson, D. Bloch, D. Bodin, J.-M. Brom, E. Conte[4], F. Drouhin[4], J.-C. Fontaine[4], D. Gelé, U. Goerlach, L. Gross, P. Juillot, A.-C. Le Bihan, Y. Patois, J. Speck, P. Van Hove

Université de Lyon, Université Claude Bernard Lyon 1, CNRS-IN2P3, Institut de Physique Nucléaire de Lyon, Villeurbanne, France
C. Baty, M. Bedjidian, J. Blaha, G. Boudoul, H. Brun, N. Chanon, R. Chierici, D. Contardo, P. Depasse, T. Dupasquier, H. El Mamouni, F. Fassi[5], J. Fay, S. Gascon, B. Ille, T. Kurca, T. Le Grand, M. Lethuillier, N. Lumb, L. Mirabito, S. Perries, M. Vander Donckt, P. Verdier

E. Andronikashvili Institute of Physics, Academy of Science, Tbilisi, Georgia
N. Djaoshvili, N. Roinishvili, V. Roinishvili

Institute of High Energy Physics and Informatization, Tbilisi State University, Tbilisi, Georgia
N. Amaglobeli

RWTH Aachen University, I. Physikalisches Institut, Aachen, Germany
R. Adolphi, G. Anagnostou, R. Brauer, W. Braunschweig, M. Edelhoff, H. Esser, L. Feld, W. Karpinski, A. Khomich, K. Klein, N. Mohr, A. Ostaptchouk, D. Pandoulas, G. Pierschel, F. Raupach, S. Schael, A. Schultz von Dratzig, G. Schwering, D. Sprenger, M. Thomas, M. Weber, B. Wittmer, M. Wlochal

RWTH Aachen University, III. Physikalisches Institut A, Aachen, Germany
O. Actis, G. Altenhöfer, W. Bender, P. Biallass, M. Erdmann, G. Fetchenhauer[1], J. Frangenheim, T. Hebbeker, G. Hilgers, A. Hinzmann, K. Hoepfner, C. Hof, M. Kirsch, T. Klimkovich, P. Kreuzer[1], D. Lanske[†], M. Merschmeyer, A. Meyer, B. Philipps, H. Pieta, H. Reithler, S.A. Schmitz, L. Sonnenschein, M. Sowa, J. Steggemann, H. Szczesny, D. Teyssier, C. Zeidler

RWTH Aachen University, III. Physikalisches Institut B, Aachen, Germany
M. Bontenackels, M. Davids, M. Duda, G. Flügge, H. Geenen, M. Giffels, W. Haj Ahmad, T. Hermanns, D. Heydhausen, S. Kalinin, T. Kress, A. Linn, A. Nowack, L. Perchalla, M. Poettgens, O. Pooth, P. Sauerland, A. Stahl, D. Tornier, M.H. Zoeller

Deutsches Elektronen-Synchrotron, Hamburg, Germany
M. Aldaya Martin, U. Behrens, K. Borras, A. Campbell, E. Castro, D. Dammann, G. Eckerlin, A. Flossdorf, G. Flucke, A. Geiser, D. Hatton, J. Hauk, H. Jung, M. Kasemann, I. Katkov, C. Kleinwort, H. Kluge, A. Knutsson, E. Kuznetsova, W. Lange, W. Lohmann, R. Mankel[1], M. Marienfeld, A.B. Meyer, S. Miglioranzi, J. Mnich, M. Ohlerich, J. Olzem, A. Parenti, C. Rosemann, R. Schmidt, T. Schoerner-Sadenius, D. Volyanskyy, C. Wissing, W.D. Zeuner[1]

University of Hamburg, Hamburg, Germany
C. Autermann, F. Bechtel, J. Draeger, D. Eckstein, U. Gebbert, K. Kaschube, G. Kaussen, R. Klanner, B. Mura, S. Naumann-Emme, F. Nowak, U. Pein, C. Sander, P. Schleper, T. Schum, H. Stadie, G. Steinbrück, J. Thomsen, R. Wolf

Institut für Experimentelle Kernphysik, Karlsruhe, Germany
J. Bauer, P. Blüm, V. Buege, A. Cakir, T. Chwalek, W. De Boer, A. Dierlamm, G. Dirkes, M. Feindt, U. Felzmann, M. Frey, A. Furgeri, J. Gruschke, C. Hackstein, F. Hartmann[1], S. Heier, M. Heinrich, H. Held, D. Hirschbuehl, K.H. Hoffmann, S. Honc, C. Jung, T. Kuhr, T. Liamsuwan, D. Martschei, S. Mueller, Th. Müller, M.B. Neuland, M. Niegel, O. Oberst, A. Oehler, J. Ott, T. Peiffer, D. Piparo, G. Quast, K. Rabbertz, F. Ratnikov, N. Ratnikova, M. Renz, C. Saout[1], G. Sartisohn, A. Scheurer, P. Schieferdecker, F.-P. Schilling, G. Schott, H.J. Simonis,

F.M. Stober, P. Sturm, D. Troendle, A. Trunov, W. Wagner, J. Wagner-Kuhr, M. Zeise, V. Zhukov[6], E.B. Ziebarth

Institute of Nuclear Physics "Demokritos", Aghia Paraskevi, Greece
G. Daskalakis, T. Geralis, K. Karafasoulis, A. Kyriakis, D. Loukas, A. Markou, C. Markou, C. Mavrommatis, E. Petrakou, A. Zachariadou

University of Athens, Athens, Greece
L. Gouskos, P. Katsas, A. Panagiotou[1]

University of Ioánnina, Ioánnina, Greece
I. Evangelou, P. Kokkas, N. Manthos, I. Papadopoulos, V. Patras, F.A. Triantis

KFKI Research Institute for Particle and Nuclear Physics, Budapest, Hungary
G. Bencze[1], L. Boldizsar, G. Debreczeni, C. Hajdu[1], S. Hernath, P. Hidas, D. Horvath[7], K. Krajczar, A. Laszlo, G. Patay, F. Sikler, N. Toth, G. Vesztergombi

Institute of Nuclear Research ATOMKI, Debrecen, Hungary
N. Beni, G. Christian, J. Imrek, J. Molnar, D. Novak, J. Palinkas, G. Szekely, Z. Szillasi[1], K. Tokesi, V. Veszpremi

University of Debrecen, Debrecen, Hungary
A. Kapusi, G. Marian, P. Raics, Z. Szabo, Z.L. Trocsanyi, B. Ujvari, G. Zilizi

Panjab University, Chandigarh, India
S. Bansal, H.S. Bawa, S.B. Beri, V. Bhatnagar, M. Jindal, M. Kaur, R. Kaur, J.M. Kohli, M.Z. Mehta, N. Nishu, L.K. Saini, A. Sharma, A. Singh, J.B. Singh, S.P. Singh

University of Delhi, Delhi, India
S. Ahuja, S. Arora, S. Bhattacharya[8], S. Chauhan, B.C. Choudhary, P. Gupta, S. Jain, S. Jain, M. Jha, A. Kumar, K. Ranjan, R.K. Shivpuri, A.K. Srivastava

Bhabha Atomic Research Centre, Mumbai, India
R.K. Choudhury, D. Dutta, S. Kailas, S.K. Kataria, A.K. Mohanty, L.M. Pant, P. Shukla, A. Topkar

Tata Institute of Fundamental Research - EHEP, Mumbai, India
T. Aziz, M. Guchait[9], A. Gurtu, M. Maity[10], D. Majumder, G. Majumder, K. Mazumdar, A. Nayak, A. Saha, K. Sudhakar

Tata Institute of Fundamental Research - HECR, Mumbai, India
S. Banerjee, S. Dugad, N.K. Mondal

Institute for Studies in Theoretical Physics & Mathematics (IPM), Tehran, Iran
H. Arfaei, H. Bakhshiansohi, A. Fahim, A. Jafari, M. Mohammadi Najafabadi, A. Moshaii, S. Paktinat Mehdiabadi, S. Rouhani, B. Safarzadeh, M. Zeinali

University College Dublin, Dublin, Ireland
M. Felcini

INFN Sezione di Bari [a], Università di Bari [b], Politecnico di Bari [c], Bari, Italy
M. Abbrescia[a,b], L. Barbone[a], F. Chiumarulo[a], A. Clemente[a], A. Colaleo[a], D. Creanza[a,c], G. Cuscela[a], N. De Filippis[a], M. De Palma[a,b], G. De Robertis[a], G. Donvito[a], F. Fedele[a], L. Fiore[a], M. Franco[a], G. Iaselli[a,c], N. Lacalamita[a], F. Loddo[a], L. Lusito[a,b], G. Maggi[a,c], M. Maggi[a], N. Manna[a,b], B. Marangelli[a,b], S. My[a,c], S. Natali[a,b], S. Nuzzo[a,b], G. Papagni[a], S. Piccolomo[a], G.A. Pierro[a], C. Pinto[a], A. Pompili[a,b], G. Pugliese[a,c], R. Rajan[a], A. Ranieri[a], F. Romano[a,c],

G. Roselli[a,b], G. Selvaggi[a,b], Y. Shinde[a], L. Silvestris[a], S. Tupputi[a,b], G. Zito[a]

INFN Sezione di Bologna [a], Universita di Bologna [b], Bologna, Italy
G. Abbiendi[a], W. Bacchi[a,b], A.C. Benvenuti[a], M. Boldini[a], D. Bonacorsi[a], S. Braibant-Giacomelli[a,b], V.D. Cafaro[a], S.S. Caiazza[a], P. Capiluppi[a,b], A. Castro[a,b], F.R. Cavallo[a], G. Codispoti[a,b], M. Cuffiani[a,b], I. D'Antone[a], G.M. Dallavalle[a,1], F. Fabbri[a], A. Fanfani[a,b], D. Fasanella[a], P. Giacomelli[a], V. Giordano[a], M. Giunta[a,1], C. Grandi[a], M. Guerzoni[a], S. Marcellini[a], G. Masetti[a,b], A. Montanari[a], F.L. Navarria[a,b], F. Odorici[a], G. Pellegrini[a], A. Perrotta[a], A.M. Rossi[a,b], T. Rovelli[a,b], G. Siroli[a,b], G. Torromeo[a], R. Travaglini[a,b]

INFN Sezione di Catania [a], Universita di Catania [b], Catania, Italy
S. Albergo[a,b], S. Costa[a,b], R. Potenza[a,b], A. Tricomi[a,b], C. Tuve[a]

INFN Sezione di Firenze [a], Universita di Firenze [b], Firenze, Italy
G. Barbagli[a], G. Broccolo[a,b], V. Ciulli[a,b], C. Civinini[a], R. D'Alessandro[a,b], E. Focardi[a,b], S. Frosali[a,b], E. Gallo[a], C. Genta[a,b], G. Landi[a,b], P. Lenzi[a,b,1], M. Meschini[a], S. Paoletti[a], G. Sguazzoni[a], A. Tropiano[a]

INFN Laboratori Nazionali di Frascati, Frascati, Italy
L. Benussi, M. Bertani, S. Bianco, S. Colafranceschi[11], D. Colonna[11], F. Fabbri, M. Giardoni, L. Passamonti, D. Piccolo, D. Pierluigi, B. Ponzio, A. Russo

INFN Sezione di Genova, Genova, Italy
P. Fabbricatore, R. Musenich

INFN Sezione di Milano-Biccoca [a], Universita di Milano-Bicocca [b], Milano, Italy
A. Benaglia[a], M. Calloni[a], G.B. Cerati[a,b,1], P. D'Angelo[a], F. De Guio[a], F.M. Farina[a], A. Ghezzi[a], P. Govoni[a,b], M. Malberti[a,b,1], S. Malvezzi[a], A. Martelli[a], D. Menasce[a], V. Miccio[a,b], L. Moroni[a], P. Negri[a,b], M. Paganoni[a,b], D. Pedrini[a], A. Pullia[a,b], S. Ragazzi[a,b], N. Redaelli[a], S. Sala[a], R. Salerno[a,b], T. Tabarelli de Fatis[a,b], V. Tancini[a,b], S. Taroni[a,b]

INFN Sezione di Napoli [a], Universita di Napoli "Federico II" [b], Napoli, Italy
S. Buontempo[a], N. Cavallo[a], A. Cimmino[a,b,1], M. De Gruttola[a,b,1], F. Fabozzi[a,12], A.O.M. Iorio[a], L. Lista[a], D. Lomidze[a], P. Noli[a,b], P. Paolucci[a], C. Sciacca[a,b]

INFN Sezione di Padova [a], Università di Padova [b], Padova, Italy
P. Azzi[a,1], N. Bacchetta[a], L. Barcellan[a], P. Bellan[a,b,1], M. Bellato[a], M. Benettoni[a], M. Biasotto[a,13], D. Bisello[a,b], E. Borsato[a,b], A. Branca[a], R. Carlin[a,b], L. Castellani[a], P. Checchia[a], E. Conti[a], F. Dal Corso[a], M. De Mattia[a,b], T. Dorigo[a], U. Dosselli[a], F. Fanzago[a], F. Gasparini[a,b], U. Gasparini[a,b], P. Giubilato[a,b], F. Gonella[a], A. Gresele[a,14], M. Gulmini[a,13], A. Kaminskiy[a,b], S. Lacaprara[a,13], I. Lazzizzera[a,14], M. Margoni[a,b], G. Maron[a,13], S. Mattiazzo[a,b], M. Mazzucato[a], M. Meneghelli[a], A.T. Meneguzzo[a,b], M. Michelotto[a], F. Montecassiano[a], M. Nespolo[a], M. Passaseo[a], M. Pegoraro[a], L. Perrozzi[a], N. Pozzobon[a,b], P. Ronchese[a,b], F. Simonetto[a,b], N. Toniolo[a], E. Torassa[a], M. Tosi[a,b], A. Triossi[a], S. Vanini[a,b], S. Ventura[a], P. Zotto[a,b], G. Zumerle[a,b]

INFN Sezione di Pavia [a], Universita di Pavia [b], Pavia, Italy
P. Baesso[a,b], U. Berzano[a], S. Bricola[a], M.M. Necchi[a,b], D. Pagano[a,b], S.P. Ratti[a,b], C. Riccardi[a,b], P. Torre[a,b], A. Vicini[a], P. Vitulo[a,b], C. Viviani[a,b]

INFN Sezione di Perugia [a], Universita di Perugia [b], Perugia, Italy
D. Aisa[a], S. Aisa[a], E. Babucci[a], M. Biasini[a,b], G.M. Bilei[a], B. Caponeri[a,b], B. Checcucci[a], N. Dinu[a], L. Fanò[a], L. Farnesini[a], P. Lariccia[a,b], A. Lucaroni[a,b], G. Mantovani[a,b], A. Nappi[a,b], A. Piluso[a], V. Postolache[a], A. Santocchia[a,b], L. Servoli[a], D. Tonoiu[a], A. Vedaee[a], R. Volpe[a,b]

INFN Sezione di Pisa [a], Universita di Pisa [b], Scuola Normale Superiore di Pisa [c], Pisa, Italy
P. Azzurri[a,c], G. Bagliesi[a], J. Bernardini[a,b], L. Berretta[a], T. Boccali[a], A. Bocci[a,c], L. Borrello[a,c], F. Bosi[a], F. Calzolari[a], R. Castaldi[a], R. Dell'Orso[a], F. Fiori[a,b], L. Foà[a,c], S. Gennai[a,c], A. Giassi[a], A. Kraan[a], F. Ligabue[a,c], T. Lomtadze[a], F. Mariani[a], L. Martini[a], M. Massa[a], A. Messineo[a,b], A. Moggi[a], F. Palla[a], F. Palmonari[a], G. Petragnani[a], G. Petrucciani[a,c], F. Raffaelli[a], S. Sarkar[a], G. Segneri[a], A.T. Serban[a], P. Spagnolo[a,1], R. Tenchini[a,1], S. Tolaini[a], G. Tonelli[a,b,1], A. Venturi[a], P.G. Verdini[a]

INFN Sezione di Roma [a], Universita di Roma "La Sapienza" [b], Roma, Italy
S. Baccaro[a,15], L. Barone[a,b], A. Bartoloni[a], F. Cavallari[a,1], I. Dafinei[a], D. Del Re[a,b], E. Di Marco[a,b], M. Diemoz[a], D. Franci[a,b], E. Longo[a,b], G. Organtini[a,b], A. Palma[a,b], F. Pandolfi[a,b], R. Paramatti[a,1], F. Pellegrino[a], S. Rahatlou[a,b], C. Rovelli[a]

INFN Sezione di Torino [a], Università di Torino [b], Università del Piemonte Orientale (Novara) [c], Torino, Italy
G. Alampi[a], N. Amapane[a,b], R. Arcidiacono[a,b], S. Argiro[a,b], M. Arneodo[a,c], C. Biino[a], M.A. Borgia[a,b], C. Botta[a,b], N. Cartiglia[a], R. Castello[a,b], G. Cerminara[a,b], M. Costa[a,b], D. Dattola[a], G. Dellacasa[a], N. Demaria[a], G. Dughera[a], F. Dumitrache[a], A. Graziano[a,b], C. Mariotti[a], M. Marone[a,b], S. Maselli[a], E. Migliore[a,b], G. Mila[a,b], V. Monaco[a,b], M. Musich[a,b], M. Nervo[a,b], M.M. Obertino[a,c], S. Oggero[a,b], R. Panero[a], N. Pastrone[a], M. Pelliccioni[a,b], A. Romero[a,b], M. Ruspa[a,c], R. Sacchi[a,b], A. Solano[a,b], A. Staiano[a], P.P. Trapani[a,b,1], D. Trocino[a,b], A. Vilela Pereira[a,b], L. Visca[a,b], A. Zampieri[a]

INFN Sezione di Trieste [a], Universita di Trieste [b], Trieste, Italy
F. Ambroglini[a,b], S. Belforte[a], F. Cossutti[a], G. Della Ricca[a,b], B. Gobbo[a], A. Penzo[a]

Kyungpook National University, Daegu, Korea
S. Chang, J. Chung, D.H. Kim, G.N. Kim, D.J. Kong, H. Park, D.C. Son

Wonkwang University, Iksan, Korea
S.Y. Bahk

Chonnam National University, Kwangju, Korea
S. Song

Konkuk University, Seoul, Korea
S.Y. Jung

Korea University, Seoul, Korea
B. Hong, H. Kim, J.H. Kim, K.S. Lee, D.H. Moon, S.K. Park, H.B. Rhee, K.S. Sim

Seoul National University, Seoul, Korea
J. Kim

University of Seoul, Seoul, Korea
M. Choi, G. Hahn, I.C. Park

Sungkyunkwan University, Suwon, Korea
S. Choi, Y. Choi, J. Goh, H. Jeong, T.J. Kim, J. Lee, S. Lee

Vilnius University, Vilnius, Lithuania
M. Janulis, D. Martisiute, P. Petrov, T. Sabonis

Centro de Investigacion y de Estudios Avanzados del IPN, Mexico City, Mexico
H. Castilla Valdez[1], A. Sánchez Hernández

Universidad Iberoamericana, Mexico City, Mexico
S. Carrillo Moreno

Universidad Autónoma de San Luis Potosí, San Luis Potosí, Mexico
A. Morelos Pineda

University of Auckland, Auckland, New Zealand
P. Allfrey, R.N.C. Gray, D. Krofcheck

University of Canterbury, Christchurch, New Zealand
N. Bernardino Rodrigues, P.H. Butler, T. Signal, J.C. Williams

National Centre for Physics, Quaid-I-Azam University, Islamabad, Pakistan
M. Ahmad, I. Ahmed, W. Ahmed, M.I. Asghar, M.I.M. Awan, H.R. Hoorani, I. Hussain, W.A. Khan, T. Khurshid, S. Muhammad, S. Qazi, H. Shahzad

Institute of Experimental Physics, Warsaw, Poland
M. Cwiok, R. Dabrowski, W. Dominik, K. Doroba, M. Konecki, J. Krolikowski, K. Pozniak[16], R. Romaniuk, W. Zabolotny[16], P. Zych

Soltan Institute for Nuclear Studies, Warsaw, Poland
T. Frueboes, R. Gokieli, L. Goscilo, M. Górski, M. Kazana, K. Nawrocki, M. Szleper, G. Wrochna, P. Zalewski

Laboratório de Instrumentação e Física Experimental de Partículas, Lisboa, Portugal
N. Almeida, L. Antunes Pedro, P. Bargassa, A. David, P. Faccioli, P.G. Ferreira Parracho, M. Freitas Ferreira, M. Gallinaro, M. Guerra Jordao, P. Martins, G. Mini, P. Musella, J. Pela, L. Raposo, P.Q. Ribeiro, S. Sampaio, J. Seixas, J. Silva, P. Silva, D. Soares, M. Sousa, J. Varela, H.K. Wöhri

Joint Institute for Nuclear Research, Dubna, Russia
I. Altsybeev, I. Belotelov, P. Bunin, Y. Ershov, I. Filozova, M. Finger, M. Finger Jr., A. Golunov, I. Golutvin, N. Gorbounov, V. Kalagin, A. Kamenev, V. Karjavin, V. Konoplyanikov, V. Korenkov, G. Kozlov, A. Kurenkov, A. Lanev, A. Makankin, V.V. Mitsyn, P. Moisenz, E. Nikonov, D. Oleynik, V. Palichik, V. Perelygin, A. Petrosyan, R. Semenov, S. Shmatov, V. Smirnov, D. Smolin, E. Tikhonenko, S. Vasil'ev, A. Vishnevskiy, A. Volodko, A. Zarubin, V. Zhiltsov

Petersburg Nuclear Physics Institute, Gatchina (St Petersburg), Russia
N. Bondar, L. Chtchipounov, A. Denisov, Y. Gavrikov, G. Gavrilov, V. Golovtsov, Y. Ivanov, V. Kim, V. Kozlov, P. Levchenko, G. Obrant, E. Orishchin, A. Petrunin, Y. Shcheglov, A. Shchetkovskiy, V. Sknar, I. Smirnov, V. Sulimov, V. Tarakanov, L. Uvarov, S. Vavilov, G. Velichko, S. Volkov, A. Vorobyev

Institute for Nuclear Research, Moscow, Russia
Yu. Andreev, A. Anisimov, P. Antipov, A. Dermenev, S. Gninenko, N. Golubev, M. Kirsanov, N. Krasnikov, V. Matveev, A. Pashenkov, V.E. Postoev, A. Solovey, A. Solovey, A. Toropin, S. Troitsky

Institute for Theoretical and Experimental Physics, Moscow, Russia
A. Baud, V. Epshteyn, V. Gavrilov, N. Ilina, V. Kaftanov†, V. Kolosov, M. Kossov[1], A. Krokhotin, S. Kuleshov, A. Oulianov, G. Safronov, S. Semenov, I. Shreyber, V. Stolin, E. Vlasov, A. Zhokin

Moscow State University, Moscow, Russia
E. Boos, M. Dubinin[17], L. Dudko, A. Ershov, A. Gribushin, V. Klyukhin, O. Kodolova, I. Lokhtin, S. Petrushanko, L. Sarycheva, V. Savrin, A. Snigirev, I. Vardanyan

P.N. Lebedev Physical Institute, Moscow, Russia
I. Dremin, M. Kirakosyan, N. Konovalova, S.V. Rusakov, A. Vinogradov

State Research Center of Russian Federation, Institute for High Energy Physics, Protvino, Russia
S. Akimenko, A. Artamonov, I. Azhgirey, S. Bitioukov, V. Burtovoy, V. Grishin[1], V. Kachanov, D. Konstantinov, V. Krychkine, A. Levine, I. Lobov, V. Lukanin, Y. Mel'nik, V. Petrov, R. Ryutin, S. Slabospitsky, A. Sobol, A. Sytine, L. Tourtchanovitch, S. Troshin, N. Tyurin, A. Uzunian, A. Volkov

Vinca Institute of Nuclear Sciences, Belgrade, Serbia
P. Adzic, M. Djordjevic, D. Jovanovic[18], D. Krpic[18], D. Maletic, J. Puzovic[18], N. Smiljkovic

Centro de Investigaciones Energéticas Medioambientales y Tecnológicas (CIEMAT), Madrid, Spain
M. Aguilar-Benitez, J. Alberdi, J. Alcaraz Maestre, P. Arce, J.M. Barcala, C. Battilana, C. Burgos Lazaro, J. Caballero Bejar, E. Calvo, M. Cardenas Montes, M. Cepeda, M. Cerrada, M. Chamizo Llatas, F. Clemente, N. Colino, M. Daniel, B. De La Cruz, A. Delgado Peris, C. Diez Pardos, C. Fernandez Bedoya, J.P. Fernández Ramos, A. Ferrando, J. Flix, M.C. Fouz, P. Garcia-Abia, A.C. Garcia-Bonilla, O. Gonzalez Lopez, S. Goy Lopez, J.M. Hernandez, M.I. Josa, J. Marin, G. Merino, J. Molina, A. Molinero, J.J. Navarrete, J.C. Oller, J. Puerta Pelayo, L. Romero, J. Santaolalla, C. Villanueva Munoz, C. Willmott, C. Yuste

Universidad Autónoma de Madrid, Madrid, Spain
C. Albajar, M. Blanco Otano, J.F. de Trocóniz, A. Garcia Raboso, J.O. Lopez Berengueres

Universidad de Oviedo, Oviedo, Spain
J. Cuevas, J. Fernandez Menendez, I. Gonzalez Caballero, L. Lloret Iglesias, H. Naves Sordo, J.M. Vizan Garcia

Instituto de Física de Cantabria (IFCA), CSIC-Universidad de Cantabria, Santander, Spain
I.J. Cabrillo, A. Calderon, S.H. Chuang, I. Diaz Merino, C. Diez Gonzalez, J. Duarte Campderros, M. Fernandez, G. Gomez, J. Gonzalez Sanchez, R. Gonzalez Suarez, C. Jorda, P. Lobelle Pardo, A. Lopez Virto, J. Marco, R. Marco, C. Martinez Rivero, P. Martinez Ruiz del Arbol, F. Matorras, T. Rodrigo, A. Ruiz Jimeno, L. Scodellaro, M. Sobron Sanudo, I. Vila, R. Vilar Cortabitarte

CERN, European Organization for Nuclear Research, Geneva, Switzerland
D. Abbaneo, E. Albert, M. Alidra, S. Ashby, E. Auffray, J. Baechler, P. Baillon, A.H. Ball, S.L. Bally, D. Barney, F. Beaudette[19], R. Bellan, D. Benedetti, G. Benelli, C. Bernet, P. Bloch, S. Bolognesi, M. Bona, J. Bos, N. Bourgeois, T. Bourrel, H. Breuker, K. Bunkowski, D. Campi, T. Camporesi, E. Cano, A. Cattai, J.P. Chatelain, M. Chauvey, T. Christiansen, J.A. Coarasa Perez, A. Conde Garcia, R. Covarelli, B. Curé, A. De Roeck, V. Delachenal, D. Deyrail, S. Di Vincenzo[20], S. Dos Santos, T. Dupont, L.M. Edera, A. Elliott-Peisert, M. Eppard, M. Favre, N. Frank, W. Funk, A. Gaddi, M. Gastal, M. Gateau, H. Gerwig, D. Gigi, K. Gill, D. Giordano, J.P. Girod, F. Glege, R. Gomez-Reino Garrido, R. Goudard, S. Gowdy, R. Guida, L. Guiducci, J. Gutleber, M. Hansen, C. Hartl, J. Harvey, B. Hegner, H.F. Hoffmann, A. Holzner, A. Honma, M. Huhtinen, V. Innocente, P. Janot, G. Le Godec, P. Lecoq, C. Leonidopoulos, R. Loos, C. Lourenço, A. Lyonnet, A. Macpherson, N. Magini, J.D. Maillefaud, G. Maire, T. Mäki, L. Malgeri, M. Mannelli, L. Masetti, F. Meijers, P. Meridiani, S. Mersi, E. Meschi, A. Meynet Cordonnier, R. Moser, M. Mulders, J. Mulon, M. Noy, A. Oh, G. Olesen, A. Onnela, T. Orimoto, L. Orsini, E. Perez, G. Perinic, J.F. Pernot, P. Petagna, P. Petiot, A. Petrilli, A. Pfeiffer, M. Pierini, M. Pimiä, R. Pintus, B. Pirollet, H. Postema, A. Racz, S. Ravat, S.B. Rew, J. Rodrigues Antunes,

G. Rolandi[21], M. Rovere, V. Ryjov, H. Sakulin, D. Samyn, H. Sauce, C. Schäfer, W.D. Schlatter, M. Schröder, C. Schwick, A. Sciaba, I. Segoni, A. Sharma, N. Siegrist, P. Siegrist, N. Sinanis, T. Sobrier, P. Sphicas[22], D. Spiga, M. Spiropulu[17], F. Stöckli, P. Traczyk, P. Tropea, J. Troska, A. Tsirou, L. Veillet, G.I. Veres, M. Voutilainen, P. Wertelaers, M. Zanetti

Paul Scherrer Institut, Villigen, Switzerland
W. Bertl, K. Deiters, W. Erdmann, K. Gabathuler, R. Horisberger, Q. Ingram, H.C. Kaestli, S. König, D. Kotlinski, U. Langenegger, F. Meier, D. Renker, T. Rohe, J. Sibille[23], A. Starodumov[24]

Institute for Particle Physics, ETH Zurich, Zurich, Switzerland
B. Betev, L. Caminada[25], Z. Chen, S. Cittolin, D.R. Da Silva Di Calafiori, S. Dambach[25], G. Dissertori, M. Dittmar, C. Eggel[25], J. Eugster, G. Faber, K. Freudenreich, C. Grab, A. Hervé, W. Hintz, P. Lecomte, P.D. Luckey, W. Lustermann, C. Marchica[25], P. Milenovic[26], F. Moortgat, A. Nardulli, F. Nessi-Tedaldi, L. Pape, F. Pauss, T. Punz, A. Rizzi, F.J. Ronga, L. Sala, A.K. Sanchez, M.-C. Sawley, V. Sordini, B. Stieger, L. Tauscher†, A. Thea, K. Theofilatos, D. Treille, P. Trüb[25], M. Weber, L. Wehrli, J. Weng, S. Zelepoukine[27]

Universität Zürich, Zurich, Switzerland
C. Amsler, V. Chiochia, S. De Visscher, C. Regenfus, P. Robmann, T. Rommerskirchen, A. Schmidt, D. Tsirigkas, L. Wilke

National Central University, Chung-Li, Taiwan
Y.H. Chang, E.A. Chen, W.T. Chen, A. Go, C.M. Kuo, S.W. Li, W. Lin

National Taiwan University (NTU), Taipei, Taiwan
P. Bartalini, P. Chang, Y. Chao, K.F. Chen, W.-S. Hou, Y. Hsiung, Y.J. Lei, S.W. Lin, R.-S. Lu, J. Schümann, J.G. Shiu, Y.M. Tzeng, K. Ueno, Y. Velikzhanin, C.C. Wang, M. Wang

Cukurova University, Adana, Turkey
A. Adiguzel, A. Ayhan, A. Azman Gokce, M.N. Bakirci, S. Cerci, I. Dumanoglu, E. Eskut, S. Girgis, E. Gurpinar, I. Hos, T. Karaman, T. Karaman, A. Kayis Topaksu, P. Kurt, G. Önengüt, G. Önengüt Gökbulut, K. Ozdemir, S. Ozturk, A. Polatöz, K. Sogut[28], B. Tali, H. Topakli, D. Uzun, L.N. Vergili, M. Vergili

Middle East Technical University, Physics Department, Ankara, Turkey
I.V. Akin, T. Aliev, S. Bilmis, M. Deniz, H. Gamsizkan, A.M. Guler, K. Öcalan, M. Serin, R. Sever, U.E. Surat, M. Zeyrek

Bogaziçi University, Department of Physics, Istanbul, Turkey
M. Deliomeroglu, D. Demir[29], E. Gülmez, A. Halu, B. Isildak, M. Kaya[30], O. Kaya[30], S. Ozkorucuklu[31], N. Sonmez[32]

National Scientific Center, Kharkov Institute of Physics and Technology, Kharkov, Ukraine
L. Levchuk, S. Lukyanenko, D. Soroka, S. Zub

University of Bristol, Bristol, United Kingdom
F. Bostock, J.J. Brooke, T.L. Cheng, D. Cussans, R. Frazier, J. Goldstein, N. Grant, M. Hansen, G.P. Heath, H.F. Heath, C. Hill, B. Huckvale, J. Jackson, C.K. Mackay, S. Metson, D.M. Newbold[33], K. Nirunpong, V.J. Smith, J. Velthuis, R. Walton

Rutherford Appleton Laboratory, Didcot, United Kingdom
K.W. Bell, C. Brew, R.M. Brown, B. Camanzi, D.J.A. Cockerill, J.A. Coughlan, N.I. Geddes, K. Harder, S. Harper, B.W. Kennedy, P. Murray, C.H. Shepherd-Themistocleous, I.R. Tomalin, J.H. Williams†, W.J. Womersley, S.D. Worm

Imperial College, University of London, London, United Kingdom
R. Bainbridge, G. Ball, J. Ballin, R. Beuselinck, O. Buchmuller, D. Colling, N. Cripps, G. Davies, M. Della Negra, C. Foudas, J. Fulcher, D. Futyan, G. Hall, J. Hays, G. Iles, G. Karapostoli, B.C. MacEvoy, A.-M. Magnan, J. Marrouche, J. Nash, A. Nikitenko[24], A. Papageorgiou, M. Pesaresi, K. Petridis, M. Pioppi[34], D.M. Raymond, N. Rompotis, A. Rose, M.J. Ryan, C. Seez, P. Sharp, G. Sidiropoulos[1], M. Stettler, M. Stoye, M. Takahashi, A. Tapper, C. Timlin, S. Tourneur, M. Vazquez Acosta, T. Virdee[1], S. Wakefield, D. Wardrope, T. Whyntie, M. Wingham

Brunel University, Uxbridge, United Kingdom
J.E. Cole, I. Goitom, P.R. Hobson, A. Khan, P. Kyberd, D. Leslie, C. Munro, I.D. Reid, C. Siamitros, R. Taylor, L. Teodorescu, I. Yaselli

Boston University, Boston, USA
T. Bose, M. Carleton, E. Hazen, A.H. Heering, A. Heister, J. St. John, P. Lawson, D. Lazic, D. Osborne, J. Rohlf, L. Sulak, S. Wu

Brown University, Providence, USA
J. Andrea, A. Avetisyan, S. Bhattacharya, J.P. Chou, D. Cutts, S. Esen, G. Kukartsev, G. Landsberg, M. Narain, D. Nguyen, T. Speer, K.V. Tsang

University of California, Davis, Davis, USA
R. Breedon, M. Calderon De La Barca Sanchez, M. Case, D. Cebra, M. Chertok, J. Conway, P.T. Cox, J. Dolen, R. Erbacher, E. Friis, W. Ko, A. Kopecky, R. Lander, A. Lister, H. Liu, S. Maruyama, T. Miceli, M. Nikolic, D. Pellett, J. Robles, M. Searle, J. Smith, M. Squires, J. Stilley, M. Tripathi, R. Vasquez Sierra, C. Veelken

University of California, Los Angeles, Los Angeles, USA
V. Andreev, K. Arisaka, D. Cline, R. Cousins, S. Erhan[1], J. Hauser, M. Ignatenko, C. Jarvis, J. Mumford, C. Plager, G. Rakness, P. Schlein[†], J. Tucker, V. Valuev, R. Wallny, X. Yang

University of California, Riverside, Riverside, USA
J. Babb, M. Bose, A. Chandra, R. Clare, J.A. Ellison, J.W. Gary, G. Hanson, G.Y. Jeng, S.C. Kao, F. Liu, H. Liu, A. Luthra, H. Nguyen, G. Pasztor[35], A. Satpathy, B.C. Shen[†], R. Stringer, J. Sturdy, V. Sytnik, R. Wilken, S. Wimpenny

University of California, San Diego, La Jolla, USA
J.G. Branson, E. Dusinberre, D. Evans, F. Golf, R. Kelley, M. Lebourgeois, J. Letts, E. Lipeles, B. Mangano, J. Muelmenstaedt, M. Norman, S. Padhi, A. Petrucci, H. Pi, M. Pieri, R. Ranieri, M. Sani, V. Sharma, S. Simon, F. Würthwein, A. Yagil

University of California, Santa Barbara, Santa Barbara, USA
C. Campagnari, M. D'Alfonso, T. Danielson, J. Garberson, J. Incandela, C. Justus, P. Kalavase, S.A. Koay, D. Kovalskyi, V. Krutelyov, J. Lamb, S. Lowette, V. Pavlunin, F. Rebassoo, J. Ribnik, J. Richman, R. Rossin, D. Stuart, W. To, J.R. Vlimant, M. Witherell

California Institute of Technology, Pasadena, USA
A. Apresyan, A. Bornheim, J. Bunn, M. Chiorboli, M. Gataullin, D. Kcira, V. Litvine, Y. Ma, H.B. Newman, C. Rogan, V. Timciuc, J. Veverka, R. Wilkinson, Y. Yang, L. Zhang, K. Zhu, R.Y. Zhu

Carnegie Mellon University, Pittsburgh, USA
B. Akgun, R. Carroll, T. Ferguson, D.W. Jang, S.Y. Jun, M. Paulini, J. Russ, N. Terentyev, H. Vogel, I. Vorobiev

University of Colorado at Boulder, Boulder, USA
J.P. Cumalat, M.E. Dinardo, B.R. Drell, W.T. Ford, B. Heyburn, E. Luiggi Lopez, U. Nauenberg, K. Stenson, K. Ulmer, S.R. Wagner, S.L. Zang

Cornell University, Ithaca, USA
L. Agostino, J. Alexander, F. Blekman, D. Cassel, A. Chatterjee, S. Das, L.K. Gibbons, B. Heltsley, W. Hopkins, A. Khukhunaishvili, B. Kreis, V. Kuznetsov, J.R. Patterson, D. Puigh, A. Ryd, X. Shi, S. Stroiney, W. Sun, W.D. Teo, J. Thom, J. Vaughan, Y. Weng, P. Wittich

Fairfield University, Fairfield, USA
C.P. Beetz, G. Cirino, C. Sanzeni, D. Winn

Fermi National Accelerator Laboratory, Batavia, USA
S. Abdullin, M.A. Afaq[1], M. Albrow, B. Ananthan, G. Apollinari, M. Atac, W. Badgett, L. Bagby, J.A. Bakken, B. Baldin, S. Banerjee, K. Banicz, L.A.T. Bauerdick, A. Beretvas, J. Berryhill, P.C. Bhat, K. Biery, M. Binkley, I. Bloch, F. Borcherding, A.M. Brett, K. Burkett, J.N. Butler, V. Chetluru, H.W.K. Cheung, F. Chlebana, I. Churin, S. Cihangir, M. Crawford, W. Dagenhart, M. Demarteau, G. Derylo, D. Dykstra, D.P. Eartly, J.E. Elias, V.D. Elvira, D. Evans, L. Feng, M. Fischler, I. Fisk, S. Foulkes, J. Freeman, P. Gartung, E. Gottschalk, T. Grassi, D. Green, Y. Guo, O. Gutsche, A. Hahn, J. Hanlon, R.M. Harris, B. Holzman, J. Howell, D. Hufnagel, E. James, H. Jensen, M. Johnson, C.D. Jones, U. Joshi, E. Juska, J. Kaiser, B. Klima, S. Kossiakov, K. Kousouris, S. Kwan, C.M. Lei, P. Limon, J.A. Lopez Perez, S. Los, L. Lueking, G. Lukhanin, S. Lusin[1], J. Lykken, K. Maeshima, J.M. Marraffino, D. Mason, P. McBride, T. Miao, K. Mishra, S. Moccia, R. Mommsen, S. Mrenna, A.S. Muhammad, C. Newman-Holmes, C. Noeding, V. O'Dell, O. Prokofyev, R. Rivera, C.H. Rivetta, A. Ronzhin, P. Rossman, S. Ryu, V. Sekhri, E. Sexton-Kennedy, I. Sfiligoi, S. Sharma, T.M. Shaw, D. Shpakov, E. Skup, R.P. Smith[†], A. Soha, W.J. Spalding, L. Spiegel, I. Suzuki, P. Tan, W. Tanenbaum, S. Tkaczyk[1], R. Trentadue[1], L. Uplegger, E.W. Vaandering, R. Vidal, J. Whitmore, E. Wicklund, W. Wu, J. Yarba, F. Yumiceva, J.C. Yun

University of Florida, Gainesville, USA
D. Acosta, P. Avery, V. Barashko, D. Bourilkov, M. Chen, G.P. Di Giovanni, D. Dobur, A. Drozdetskiy, R.D. Field, Y. Fu, I.K. Furic, J. Gartner, D. Holmes, B. Kim, S. Klimenko, J. Konigsberg, A. Korytov, K. Kotov, A. Kropivnitskaya, T. Kypreos, A. Madorsky, K. Matchev, G. Mitselmakher, Y. Pakhotin, J. Piedra Gomez, C. Prescott, V. Rapsevicius, R. Remington, M. Schmitt, B. Scurlock, D. Wang, J. Yelton

Florida International University, Miami, USA
C. Ceron, V. Gaultney, L. Kramer, L.M. Lebolo, S. Linn, P. Markowitz, G. Martinez, J.L. Rodriguez

Florida State University, Tallahassee, USA
T. Adams, A. Askew, H. Baer, M. Bertoldi, J. Chen, W.G.D. Dharmaratna, S.V. Gleyzer, J. Haas, S. Hagopian, V. Hagopian, M. Jenkins, K.F. Johnson, E. Prettner, H. Prosper, S. Sekmen

Florida Institute of Technology, Melbourne, USA
M.M. Baarmand, S. Guragain, M. Hohlmann, H. Kalakhety, H. Mermerkaya, R. Ralich, I. Vodopiyanov

University of Illinois at Chicago (UIC), Chicago, USA
B. Abelev, M.R. Adams, I.M. Anghel, L. Apanasevich, V.E. Bazterra, R.R. Betts, J. Callner, M.A. Castro, R. Cavanaugh, C. Dragoiu, E.J. Garcia-Solis, C.E. Gerber, D.J. Hofman, S. Khalatian, C. Mironov, E. Shabalina, A. Smoron, N. Varelas

The University of Iowa, Iowa City, USA
U. Akgun, E.A. Albayrak, A.S. Ayan, B. Bilki, R. Briggs, K. Cankocak[36], K. Chung, W. Clarida, P. Debbins, F. Duru, F.D. Ingram, C.K. Lae, E. McCliment, J.-P. Merlo, A. Mestvirishvili, M.J. Miller, A. Moeller, J. Nachtman, C.R. Newsom, E. Norbeck, J. Olson, Y. Onel, F. Ozok, J. Parsons, I. Schmidt, S. Sen, J. Wetzel, T. Yetkin, K. Yi

Johns Hopkins University, Baltimore, USA
B.A. Barnett, B. Blumenfeld, A. Bonato, C.Y. Chien, D. Fehling, G. Giurgiu, A.V. Gritsan, Z.J. Guo, P. Maksimovic, S. Rappoccio, M. Swartz, N.V. Tran, Y. Zhang

The University of Kansas, Lawrence, USA
P. Baringer, A. Bean, O. Grachov, M. Murray, V. Radicci, S. Sanders, J.S. Wood, V. Zhukova

Kansas State University, Manhattan, USA
D. Bandurin, T. Bolton, K. Kaadze, A. Liu, Y. Maravin, D. Onoprienko, I. Svintradze, Z. Wan

Lawrence Livermore National Laboratory, Livermore, USA
J. Gronberg, J. Hollar, D. Lange, D. Wright

University of Maryland, College Park, USA
D. Baden, R. Bard, M. Boutemeur, S.C. Eno, D. Ferencek, N.J. Hadley, R.G. Kellogg, M. Kirn, S. Kunori, K. Rossato, P. Rumerio, F. Santanastasio, A. Skuja, J. Temple, M.B. Tonjes, S.C. Tonwar, T. Toole, E. Twedt

Massachusetts Institute of Technology, Cambridge, USA
B. Alver, G. Bauer, J. Bendavid, W. Busza, E. Butz, I.A. Cali, M. Chan, D. D'Enterria, P. Everaerts, G. Gomez Ceballos, K.A. Hahn, P. Harris, S. Jaditz, Y. Kim, M. Klute, Y.-J. Lee, W. Li, C. Loizides, T. Ma, M. Miller, S. Nahn, C. Paus, C. Roland, G. Roland, M. Rudolph, G. Stephans, K. Sumorok, K. Sung, S. Vaurynovich, E.A. Wenger, B. Wyslouch, S. Xie, Y. Yilmaz, A.S. Yoon

University of Minnesota, Minneapolis, USA
D. Bailleux, S.I. Cooper, P. Cushman, B. Dahmes, A. De Benedetti, A. Dolgopolov, P.R. Dudero, R. Egeland, G. Franzoni, J. Haupt, A. Inyakin[37], K. Klapoetke, Y. Kubota, J. Mans, N. Mirman, D. Petyt, V. Rekovic, R. Rusack, M. Schroeder, A. Singovsky, J. Zhang

University of Mississippi, University, USA
L.M. Cremaldi, R. Godang, R. Kroeger, L. Perera, R. Rahmat, D.A. Sanders, P. Sonnek, D. Summers

University of Nebraska-Lincoln, Lincoln, USA
K. Bloom, B. Bockelman, S. Bose, J. Butt, D.R. Claes, A. Dominguez, M. Eads, J. Keller, T. Kelly, I. Kravchenko, J. Lazo-Flores, C. Lundstedt, H. Malbouisson, S. Malik, G.R. Snow

State University of New York at Buffalo, Buffalo, USA
U. Baur, I. Iashvili, A. Kharchilava, A. Kumar, K. Smith, M. Strang

Northeastern University, Boston, USA
G. Alverson, E. Barberis, O. Boeriu, G. Eulisse, G. Govi, T. McCauley, Y. Musienko[38], S. Muzaffar, I. Osborne, T. Paul, S. Reucroft, J. Swain, L. Taylor, L. Tuura

Northwestern University, Evanston, USA
A. Anastassov, B. Gobbi, A. Kubik, R.A. Ofierzynski, A. Pozdnyakov, M. Schmitt, S. Stoynev, M. Velasco, S. Won

University of Notre Dame, Notre Dame, USA
L. Antonelli, D. Berry, M. Hildreth, C. Jessop, D.J. Karmgard, T. Kolberg, K. Lannon, S. Lynch,

N. Marinelli, D.M. Morse, R. Ruchti, J. Slaunwhite, J. Warchol, M. Wayne

The Ohio State University, Columbus, USA
B. Bylsma, L.S. Durkin, J. Gilmore[39], J. Gu, P. Killewald, T.Y. Ling, G. Williams

Princeton University, Princeton, USA
N. Adam, E. Berry, P. Elmer, A. Garmash, D. Gerbaudo, V. Halyo, A. Hunt, J. Jones, E. Laird, D. Marlow, T. Medvedeva, M. Mooney, J. Olsen, P. Piroué, D. Stickland, C. Tully, J.S. Werner, T. Wildish, Z. Xie, A. Zuranski

University of Puerto Rico, Mayaguez, USA
J.G. Acosta, M. Bonnett Del Alamo, X.T. Huang, A. Lopez, H. Mendez, S. Oliveros, J.E. Ramirez Vargas, N. Santacruz, A. Zatzerklyany

Purdue University, West Lafayette, USA
E. Alagoz, E. Antillon, V.E. Barnes, G. Bolla, D. Bortoletto, A. Everett, A.F. Garfinkel, Z. Gecse, L. Gutay, N. Ippolito, M. Jones, O. Koybasi, A.T. Laasanen, N. Leonardo, C. Liu, V. Maroussov, P. Merkel, D.H. Miller, N. Neumeister, A. Sedov, I. Shipsey, H.D. Yoo, Y. Zheng

Purdue University Calumet, Hammond, USA
P. Jindal, N. Parashar

Rice University, Houston, USA
V. Cuplov, K.M. Ecklund, F.J.M. Geurts, J.H. Liu, D. Maronde, M. Matveev, B.P. Padley, R. Redjimi, J. Roberts, L. Sabbatini, A. Tumanov

University of Rochester, Rochester, USA
B. Betchart, A. Bodek, H. Budd, Y.S. Chung, P. de Barbaro, R. Demina, H. Flacher, Y. Gotra, A. Harel, S. Korjenevski, D.C. Miner, D. Orbaker, G. Petrillo, D. Vishnevskiy, M. Zielinski

The Rockefeller University, New York, USA
A. Bhatti, L. Demortier, K. Goulianos, K. Hatakeyama, G. Lungu, C. Mesropian, M. Yan

Rutgers, the State University of New Jersey, Piscataway, USA
O. Atramentov, E. Bartz, Y. Gershtein, E. Halkiadakis, D. Hits, A. Lath, K. Rose, S. Schnetzer, S. Somalwar, R. Stone, S. Thomas, T.L. Watts

University of Tennessee, Knoxville, USA
G. Cerizza, M. Hollingsworth, S. Spanier, Z.C. Yang, A. York

Texas A&M University, College Station, USA
J. Asaadi, A. Aurisano, R. Eusebi, A. Golyash, A. Gurrola, T. Kamon, C.N. Nguyen, J. Pivarski, A. Safonov, S. Sengupta, D. Toback, M. Weinberger

Texas Tech University, Lubbock, USA
N. Akchurin, L. Berntzon, K. Gumus, C. Jeong, H. Kim, S.W. Lee, S. Popescu, Y. Roh, A. Sill, I. Volobouev, E. Washington, R. Wigmans, E. Yazgan

Vanderbilt University, Nashville, USA
D. Engh, C. Florez, W. Johns, S. Pathak, P. Sheldon

University of Virginia, Charlottesville, USA
D. Andelin, M.W. Arenton, M. Balazs, S. Boutle, M. Buehler, S. Conetti, B. Cox, R. Hirosky, A. Ledovskoy, C. Neu, D. Phillips II, M. Ronquest, R. Yohay

Wayne State University, Detroit, USA
S. Gollapinni, K. Gunthoti, R. Harr, P.E. Karchin, M. Mattson, A. Sakharov

University of Wisconsin, Madison, USA
M. Anderson, M. Bachtis, J.N. Bellinger, D. Carlsmith, I. Crotty[1], S. Dasu, S. Dutta, J. Efron, F. Feyzi, K. Flood, L. Gray, K.S. Grogg, M. Grothe, R. Hall-Wilton[1], M. Jaworski, P. Klabbers, J. Klukas, A. Lanaro, C. Lazaridis, J. Leonard, R. Loveless, M. Magrans de Abril, A. Mohapatra, G. Ott, G. Polese, D. Reeder, A. Savin, W.H. Smith, A. Sourkov[40], J. Swanson, M. Weinberg, D. Wenman, M. Wensveen, A. White

†: Deceased
1: Also at CERN, European Organization for Nuclear Research, Geneva, Switzerland
2: Also at Universidade Federal do ABC, Santo Andre, Brazil
3: Also at Soltan Institute for Nuclear Studies, Warsaw, Poland
4: Also at Université de Haute-Alsace, Mulhouse, France
5: Also at Centre de Calcul de l'Institut National de Physique Nucleaire et de Physique des Particules (IN2P3), Villeurbanne, France
6: Also at Moscow State University, Moscow, Russia
7: Also at Institute of Nuclear Research ATOMKI, Debrecen, Hungary
8: Also at University of California, San Diego, La Jolla, USA
9: Also at Tata Institute of Fundamental Research - HECR, Mumbai, India
10: Also at University of Visva-Bharati, Santiniketan, India
11: Also at Facolta' Ingegneria Universita' di Roma "La Sapienza", Roma, Italy
12: Also at Università della Basilicata, Potenza, Italy
13: Also at Laboratori Nazionali di Legnaro dell' INFN, Legnaro, Italy
14: Also at Università di Trento, Trento, Italy
15: Also at ENEA - Casaccia Research Center, S. Maria di Galeria, Italy
16: Also at Warsaw University of Technology, Institute of Electronic Systems, Warsaw, Poland
17: Also at California Institute of Technology, Pasadena, USA
18: Also at Faculty of Physics of University of Belgrade, Belgrade, Serbia
19: Also at Laboratoire Leprince-Ringuet, Ecole Polytechnique, IN2P3-CNRS, Palaiseau, France
20: Also at Alstom Contracting, Geneve, Switzerland
21: Also at Scuola Normale e Sezione dell' INFN, Pisa, Italy
22: Also at University of Athens, Athens, Greece
23: Also at The University of Kansas, Lawrence, USA
24: Also at Institute for Theoretical and Experimental Physics, Moscow, Russia
25: Also at Paul Scherrer Institut, Villigen, Switzerland
26: Also at Vinca Institute of Nuclear Sciences, Belgrade, Serbia
27: Also at University of Wisconsin, Madison, USA
28: Also at Mersin University, Mersin, Turkey
29: Also at Izmir Institute of Technology, Izmir, Turkey
30: Also at Kafkas University, Kars, Turkey
31: Also at Suleyman Demirel University, Isparta, Turkey
32: Also at Ege University, Izmir, Turkey
33: Also at Rutherford Appleton Laboratory, Didcot, United Kingdom
34: Also at INFN Sezione di Perugia; Universita di Perugia, Perugia, Italy
35: Also at KFKI Research Institute for Particle and Nuclear Physics, Budapest, Hungary
36: Also at Istanbul Technical University, Istanbul, Turkey
37: Also at University of Minnesota, Minneapolis, USA
38: Also at Institute for Nuclear Research, Moscow, Russia
39: Also at Texas A&M University, College Station, USA
40: Also at State Research Center of Russian Federation, Institute for High Energy Physics, Protvino, Russia